MIDKINE rewires the melanoma microenvironment towards a tolerogenic and immune resistant state

Daniela Cerezo-Wallis[1], Marta Contreras-Alcalde[1], Kevin Troulé[2], Xavier Catena[1], Cynthia Mucientes[1], Tonantzin G. Calvo[1], Estela Cañón[1], Cristina Tejedo[1], Paula C. Pennacchi[1], Sabrina Hogan[3], Peter Kölblinger[3], Héctor Tejero[2], Andrew X. Chen[4], Nuria Ibarz[5], Osvaldo Graña-Castro[2], Lola Martinez[5], Javier Muñoz[6], Pablo Ortiz-Romero[7], José L Rodriguez-Peralto[8], Gonzalo Gómez-López[2], Fátima Al-Shahrour[2], Raúl Rabadán[4], Mitchell P. Levesque[3], David Olmeda[1*] and María S. Soengas[1*].

[1]Melanoma Laboratory, Molecular Oncology Programme, Spanish National Cancer Research Centre (CNIO), Madrid 28049, Spain; [2]Bioinformatics Unit, CNIO. [3]Department of Dermatology, University of Zurich Hospital, Zurich, Switzerland. [4]Flow Cytometry Unit, Biotechnology Programme, CNIO. [5]Proteomics Unit, Biotechnology Programme, CNIO and ProteoRed-ISCIII. [6]Program for Mathematical Genomics, Department of Systems Biology, Department of Biomedical Informatics, Columbia University College of Physicians & Surgeons, New York, US. [7] Dermatology Service, Hospital 12 de Octubre, Universidad Complutense Madrid Medical School, 28041, Spain.[8]Instituto de Investigación i+12, Hospital 12 de Octubre, Universidad Complutense Madrid Medical School, 28041, Spain. [9]Pathology Service, Hospital 12 de Octubre, Universidad Complutense Madrid Medical School, 28041, Spain.

***Correspondence**: msoengas@cnio.es, dolmeda@cnio.es

Keywords: MIDKINE, melanoma, secretome, immunotherapy, PDL1, PD1, tumour-associated macrophages, inflammation.

Abbreviations: BMDM, bone marrow derived macrophages; DFS, disease free survival; GOF, Gain-of-function; ICB: Immune checkpoint blockade; IHC: immunohistochemistry; LC-MS/MS: Liquid Chromatography with tandem Mass Spectrometry; LOF, loss-of-function; LPS: lipopolysaccharide; MDK, Midkine; NK, Natural killer cells; OS, Overall survival; OVA: ovalbumin; ssGSEA, single sample gene set enrichment analyses; TAM, Tumour-associated macrophages; UMAP, Uniform manifold approximation and projection plots.

ABSTRACT

An open question in aggressive cancers such as melanoma is how malignant cells can shift the immune system to pro-tumourigenic functions. Here we identify Midkine (MDK) as a melanoma-secreted driver of an “inflamed”, but immune evasive, microenvironment that defines poor patient prognosis and resistance to immune checkpoint blockade. Mechanistically, MDK was found to control the transcriptome of melanoma cells allowing for a coordinated activation of NF-κB and downregulation of interferon-associated pathways. The resulting MDK-modulated secretome educated macrophages towards tolerant phenotypes that promoted $CD8^+$-T cell dysfunction. In contrast, genetic targeting of MDK sensitized melanoma cells to anti-PD1/PDL1 treatment. Emphasizing the translational relevance of these findings, the expression profile of MDK-depleted tumours was enriched in key indicators of good response to immune checkpoint blockers in independent patient cohorts. Together, these data reveal that MDK acts as an internal modulator of autocrine and paracrine signals that maintain immune suppression in aggressive melanomas.

INTRODUCTION

The immune system is long-known as a double-edged sword in oncology for its potential to favour or to block cancer development[1,2]. This duality has complicated the identification of immune modulators as prognostic indicators or as targets for therapeutic intervention[1]. Malignant melanoma is a disease where defining endogenous activators or brakes of the immune system is particularly relevant. In this disease, inhibition of immune checkpoints such as PD1, PDL1 or CTLA4 is providing unprecedented response rates especially in combination with targeted therapy[3]. Unfortunately, a fraction of patients still succumbs to the disease[3]. Therefore, large efforts are being dedicated to uncover biomarkers that define resistance to immune modulators[4]. However, reported signatures are recognized to be highly heterogeneous[5-9], and how melanoma cells remodel the immune microenvironment is still not well understood[9].

Dissecting feedback loops that connect melanoma cells and different components of the immune system has also important implications in separating “cold” versus “hot” tumours. Immunologically “cold” lesions have been primarily associated with tumour exclusion of cytotoxic $CD8^+$ T cells[10]. However, tumours with infiltrated $CD8^+$ T cells may still fail to respond to immune checkpoint blockade (ICB) if these cells are dysfunctional or become exhausted[11]. An inflamed, but still immunosuppressive microenvironment can be potentially fuelled by various myeloid cells, particularly tumour-associated macrophages (TAMs)[12,13]. Drivers of these different immunomodulatory scenarios are not well defined[14].

We have previously identified the growth factor Midkine (MDK) as a melanoma-secreted factor with key roles in the preparation of premetastatic niches[15]. The extent to which MDK controls the immune system in melanoma is unknown. Moreover,

although MDK is expressed in a variety of neoplasms[16-19], its specific contribution to tumour-associated inflammation may be context-dependent. Thus, MDK has been found to support gastric cancer progression in part by inhibiting the cytotoxic activity of natural killer cells (NK)[20], promote low-grade gliomas by unconventional $CD8^+$ T cell activation[21], or favour hepatocarcinoma by inhibiting pro-apoptotic effects of TRAIL in tumour cells[22]. In contrast, MDK has also been found induced by pro-inflammatory cytokines such as IL-2 or IFN-γ[16], which represent classical anticancer agents[23]. Similarly, MDK can be upregulated in a variety of autoimmune diseases[16,24,25], where it acts as a potent recruiter of leukocytes[26] that ultimately promote cytotoxic T cell activation[27]. Here, we set to dissect the impact of MDK in the transcriptome and secretome of melanoma cells, and its potential therapeutic impact in the context of immunomodulation.

RESULTS

MDK-associated gene expression profile identifies patients with poor prognosis in melanoma and other tumour types

Gain-of-function (GOF) and loss-of-function (LOF) analyses were performed in melanoma cells, to define downstream effectors of MDK by RNA-sequencing (RNA-seq) and by Liquid Chromatography-Tandem Mass Spectrometry (LC-MS/MS) as summarized in **Fig. 1a**. These analyses were complemented with histopathological characterization of patient biopsies, functional studies in cellular and murine systems, and expression analyses in patient cohorts (**Fig. 1a**). We pursued these –omic studies instead of just following *MDK* mRNA expression as we found this not to be predictive of overall survival in large patient cohorts (see for the metastatic melanoma specimens

of the Cancer Genome Atlas, TCGA[28], in **Extended Fig. 1a**). This was consistent with our previous report that MDK mRNA expression and secretion are not strictly correlated[15].

For LOF, MDK was depleted in SK-Mel-147 (a melanoma cell line with high MDK levels and inherent metastatic potential)[15]. GOF studies were performed by expressing MDK in otherwise MDK-negative WM164 melanoma cells[15]. Differentially expressed genes found by RNAseq (see **Extended Fig. 1b** and **Supplementary Table 1 and 2**), were then assessed by single-sample gene set enrichment analysis (ssGSEA) in the TCGA metastatic melanoma dataset. The enrichment of the LOF or GOF expression profiles was then plotted for each patient, revealing high linearity as depicted in **Fig. 1b** (controls to rule out sample size bias using 10,000 randomly generated expression profiles are shown in **Extended Fig. 1c-f**).

Patient prognosis was then interrogated as a function of enrichment of the complete datasets identified for MDK-LOF or MDK-GOF associated profiles (individual genes were not prognostic as shown in **Supplementary Table 3**). Patient populations within the top and bottom 15th percentiles in this GOF/LOF enrichment, herein referred to $MDK^{High\text{-}P}$ and $MDK^{Low\text{-}P}$, respectively (**Fig 1b**), were found to have a differential overall survival (**Fig. 1c**). Interestingly, supporting a broad physiological relevance of MDK, we found the $MDK^{High\text{-}P}$ vs $MDK^{Low\text{-}P}$ scoring separated patient populations with significantly different prognosis not only in TCGA datasets for melanoma (**Fig. 1c**), but also in lung squamous cell carcinoma (LUSC), glioblastoma (GBM), and kidney renal clear carcinoma (KIRC) (**Extended Fig. 1g**; see multivariate analyses in **Supplementary Table 4**).

Distinct immune profiling in $MDK^{High\text{-}P}$ and $MDK^{Low\text{-}P}$ patient populations.

GSEA using Molecular Signature Databases (MSigDB)[29] revealed that MDK$^{High\text{-}P}$ and MDK$^{Low\text{-}P}$ patients have a consistent differing expression of genes involved in extracellular matrix remodelling, metabolism, cell signalling, and vasculogenesis (**Fig. 1d, Supplementary Table 5**). Importantly, these gene expression changes were not a mere reflection of a high proliferation rate (**Extended Fig. E2a**), a typical cofounder in large patient cohorts[30]. Moreover, GSEA also uncovered a variety of signalling cascades related to the immune system that were differentially deregulated in MDK$^{High\text{-}P}$ vs MDK$^{Low\text{-}P}$ melanomas (**Fig. 1d,e**). These included multiple genes involved in innate and adaptive immunity, cytokine secretion and inflammation, not previously linked to MDK (**Fig. 1e**; see **Supplementary Tables 5 and 6**).

Deconvolution by 'Estimation of STromal and Immune cells in MAlignant Tumours using Expression data' (ESTIMATE)[31] and immunogenomic data from TCGA[32] showed an increased immune score enriched for leukocyte content in MDK$^{High\text{-}P}$ TCGA metastatic melanomas (**Extended Fig. 2b**). Intriguingly, and in contrast to reported pro-inflammatory functions of MDK in degenerative diseases[16,33], MDK$^{High\text{-}P}$ patient samples had no evidence of enriched IFN-γ scoring (**Fig. 1f, left**). Instead, they showed a high TGF-β score (**Fig. 1f, right**), high *IL13* mRNA, and a trend for increased *IL10* mRNA (**Fig. 1g**), characteristic of immunosuppressive backgrounds[1,2]. A more detailed deconvolution of 16 immune cell types with CIBERSORT[34] showed significantly enriched scores for Tregs, and more notably, for macrophages in MDK$^{High\text{-}P}$ vs MDK$^{Low\text{-}P}$ melanomas (**Fig. 1h**; **Extended Fig. 2c**). This MDK$^{High\text{-}P}$-associated enrichment of macrophage signatures was confirmed by GSEA in other macrophage-associated gene sets[12] (**Fig. 1j**), and by direct single cell RNA seq in an independent cohort of melanoma patients (**Extended Fig. 2d,e**). Interestingly, high scores for TGF-β, Tregs, and macrophages were also found for MDK$^{High\text{-}P}$ patient populations in glioblastoma,

lung squamous cell carcinoma, and kidney renal clear carcinoma (**Extended Fig. 2f**), supporting physiologically-relevant roles of MDK in immune suppression.

Macrophages constitute the most abundant immune cell populations in aggressive cancers[13] and can contribute to the resistance to ICB[13,35]. Histopathological analyses in a cohort of stage III melanoma patients (n=96) revealed a positive correlation of MDK with the characteristic tumour-associated macrophage marker CD163[12] (Extended **Fig. 2g,h**). Multiparametric analyses showed positive correlation between MDK and ulceration (Extended **Fig. 2h**), a process also associated with immune deregulation[36].

Altogether, these data suggest that MDK-associated gene expression can separate distinct populations within the TCGA-dataset with a differing immunogenic profile.

The MDK-driven tumour secretome promotes immune tolerant phenotypes in myeloid cells

To assess immunossupressive functions of MDK in vivo, we generated tumour implants with MDK-negative human and mouse melanoma cell lines (WM164 and B16F1, respectively), where MDK was transduced by lentiviral vectors (GOF studies). MDK expression did not overly affect tumour growth in these settings as we previously reported[15]. This allowed us to compare cell composition within samples of equivalent lesion size. In both xenograft models (human and murine melanoma cells) MDK expression was found associated with a marked accumulation of cells positive for $Arg1^{+}$, a classical marker of immunosuppressive myeloid cells in mice[13] (**Fig. 2a-c**; **Extended Fig. 3a,b**). This was also the case for other characteristic markers of TAMs[37,38] such as inducible nitric oxide synthase (iNOS) and YM1 (chitinase-3-like protein 1 (**Extended Fig. 3a**).

To characterize immunomodulatory roles of MDK in more detail, we performed additional GOF in B16F1 and in various derivatives of YUMM cell lines[39], which we found with moderate or low *MDK* levels (**Extended Fig. 3c,d**). In parallel, we performed a converse LOF study, depleting MDK in the high-expressing murine B16R2L and the human SK-Mel-147 (**Extended Fig. 3c,d**). Immune profiles were analysed from the corresponding mouse xenografts by flow cytometry (see **Extended Fig. 3e** and **Extended Fig. 3f,g**). Tumour implants were excised at sizes >500 mm^3 to assess bulky lesions, or <200 mm^3 to characterize earlier events. In the large tumours, depletion of MDK reduced the fraction of $CD11b^+$ myeloid cells (**Fig. 2d**)**.** Instead, GOF induced $CD11b^+$ cells (**Fig. 2e;** see also **Extended Fig. 4a**), which were found to express $Ly6C^{high}Ly6G^-$ (**Fig. 2f**) and Arg1 (**Fig. 2g**). MDK also induced Arg1 in $CD11b^+F4/80^{high}$ cells characteristic of TAMs (**Fig. 2h**) but not in granulocytic/neutrophil $CD11b^+Ly6G^+Ly6C^{int}$ cells (**Extended Fig. 4b**). More complete immunophenotyping of MDK-GOF tumours at early time points of tumour growth (**Fig. 2i** and **Extended Fig. 4c**) revealed an infiltration of monocytes (identified as $CD11b^+Ly6C^+Ly6G^-F4/80^-$) and Tregs ($CD3^+CD4^+CD25^+FoxP3^+$), with a decreased conventional type 2 dendritic cells (DC2; $CD11b^+CD11c^+MHCII^+CD24^+CD103^-F4/80^-$), all consistent with a tolerant immunosuppressive background. At this early time point, mature tumour-associated macrophages ($CD11b^+Ly6G^-F4/80^+$) were not yet induced (**Extended Fig. 4c**), but already expressed Arg1 (**Extended Fig. 4d**). LOF, in turn, showed an opposing phenotype (**Extended Fig. 4e, f**). The induction of Arg1 found by flow cytometry in MDK-GOF was confirmed by analyses of mRNA expression (see for RAW264.7 and fresh bone marrow-derived macrophages (BMDM) in **Fig. 2j**). Of note, purified MDK was sufficient to induce Arg1 at the protein and mRNA level in BMDM (**Fig. 2k, l**), although this effect was significantly less potent than in the presence of the complete secretome of melanoma cells (**Fig. 2m**). Consistent with these data, depletion of MDK

in SK-Mel-147 resulted in a secretome that failed to induce Arg1 in murine macrophages (**Fig. 2n**) and other tumor-associated markers in human macrophages (**Fig. 2o**). Together, these support a mode of action whereby MDK acts in an autocrine manner on melanoma cells to induce the secretion of immune cell chemoattractants and modulators. These, in turn, may act in a paracrine level, recruiting and polarizing macrophages towards immunosuppressive phenotypes.

Transcriptomic and proteomic analyses identify networks of tumour promoting and immunosuppressive signals driven by MDK

RNA sequencing data from WM164 vs its MDK-transduced isogenic pair were analysed by GSEA using the "Hallmark" gene set collection, as this includes well-defined biological processes[29]. A spectrum of stress response programs were found to respond to MDK increase (**Extended Fig. 5a**). The most enriched, however was TNFα signalling via NF-κB (**Fig. 3a and Extended Fig. 5a**), characteristically linked to tumour promotion[2] in the context of the classical immune suppressor TGF-β, also induced by MDK (**Extended Fig. 5a**).

Quantitative proteomics by LC-MS/MS (**Fig. 3b, Extended Fig. 5b**) and subsequent network analyses by STRING[40] (**Fig. 3c**) identified a variety of immune-related factors in the secretome of cells overexpressing MDK. Examples included S100A9/A8, CCL2, LIF or MMP1/8 (**Fig. 3c**), which although with a complex regulation[41-44], they are highly interrelated and connected to NF-κB and TNF-α (**Fig 3c**). In fact, a query using the ChEA 2016 database (generated from genome-wide analyses of transcription factors)[45] revealed RELA (NF-κB p65 subunit) as the top candidate transcription factor

predicted to control the secreted factors regulated transcriptionally by MDK (**Extended Fig. 6a**).

A direct role of MDK on NF-κB activation in melanoma cells was demonstrated by the effect of recombinant MDK on p65 phosphorylation (**Extended Fig. 6b**), and by reporter assays in a total of 7 cell lines from human and mouse melanomas, as well as from glioma and lung squamous cancer cell carcinomas (**Fig. 3d**). Consequently, MDK overexpression induced key downstream targets of the NF-κB signalling pathway, both in human cancer cell lines (WM164, A549 and U87; **Fig. 3e**) and the different murine melanoma cell lines tested (YUMM2.1, **Fig. 3f;** and YUMM2.1, YUMM1.1 and YUMMER 1.7, **Fig. 3g**). In turn, MDK depletion reduced NF-κB targets (**Fig. 3h**), inasmuch as the classical NF-κB inhibitor IKK-2i/TPCA-1 (see examples for *IL6* or *TNF* mRNA in **Fig. 3i**).

A corollary of the results above is that inhibition of NF-κB may blunt the ability of MDK-expressing melanoma cells to shift macrophage polarization towards immune suppressive features. We demonstrated this to be the case by interfering with NF-κB activation in melanoma cells, either pharmacologically (**Fig. 3j**) or by means of siRNA for RelA (**Fig. 3k**; see **Extended Fig. 6d,e** for controls for the efficiency of the knock down without affecting melanoma cell viability, respectively). To further assess the impact of MDK in macrophage polarization, we focused on the S100A8 and S100A9 immunomodulators, as examples of the most upregulated factors in the MDK-modulated secretome we had found linked to NF-κB (**Fig. 3c**). Importantly, anti-calprotectin, an antibody that blocks S100A8/A9 dimers[43], compromised the ability of the MDK-driven secretome to promote the induction of *Arg1* and *IL6* in BMDM (**Extended Fig. 6c**).

Overall, these data revealed interconnected gene networks controlled by MDK at the transcriptomic level (in part via NF-κB), ultimately resulting in a secretome enriched in factors that promote immune tolerance.

MDK drives resistance to immune checkpoint blockade

To assess the potential therapeutic impact of MDK-driven immunomodulation, we performed a classical T cell-dependent vaccination assay *in vivo*[46] for the killing of ovalbumin $(OVA)^{GFP}$ expressing B16F10 melanoma cells (see schematic in **Extended Fig. 7a**). The efficacy of vaccination was confirmed by monitoring anti-OVA IgG1 production (**Fig. 4a**). However, while B16F10-OVA-Control bearing animals responded efficiently to the immunization (i.e. tumour growth reduced by over 80%), this was not the case for the B16F10-OVA-MDK counterparts (**Fig. 4b**). This impaired response in MDK-expressing tumours was accompanied by an increase of $CD11b^+$ myeloid cells (including $F4/80^+$) as defined by flow cytometry (**Fig. 4c**) and histologically (**Extended Fig. 7b**), but with an impaired $CD8^+$ T recruitment (**Fig. 4c**).

Next, we questioned whether MDK expression could also impinge on the resistance to immune checkpoint blockade (ICB) in mice. To this end, we tested anti-PD1 or anti-PDL1 antibodies (αPD1 or αPDL1, respectively). As shown in **Extended Fig. 7c,d**, αPD1 (clone RMP1-14, 10 mg/Kg) reduced by nearly 90% the growth of B16F10-OVA tumours (tested here for their high immunogenicity and strong response to ICB[47]). Instead, the MDK-overexpressing counterparts were significantly more resistant, still recruiting F4/80 macrophages and Tregs, but not $CD8^+$ T cells (**Extended Fig. 7d**). This inceased resistance to αPD1 of MDK-expressing melanoma tumors was counteracted by a small molecule inhibitor of MDK (**Fig. 4d**), highlighting the

therapeutic potential of this protein. Similar protective effects of MDK were also found for treatment with αPDL1 (**Extended Fig. 7e,f** and data not shown).

Once defined the response of high MDK-expressors, we tested the opposing scenario, namely, response to αPD1 when MDK is blocked (**Extended Fig. 3c**). We used B16R2L as this cell line is highly metastatic and has a fast tumour growth *in vivo* (see individual growth plots and their average in **Extended Fig. 8a,b**; red curves), with the consequent short-term survival of host animals (**Fig 4e**, red curve). These B16R2L tumours had a mild response to αPD1, but no mice survived beyond 45 days after implantation (**Fig. 4e**, orange; see **Extended Fig. 8a,b** for detail). Depletion of MDK in B16R2L delayed growth (**Fig. 4e**, **Extended Fig. 8a,b;** blue) and importantly, it significantly enhanced αPD1 response in all mice tested (**Fig. 4e, Extended Fig. 8b,** green).

RNAseq in bulk tumours of B16R2L implants revealed that shMDK induced by itself an enrichment of "TNF-α signalling via NFκB", but together with potent antitumoural pathways related to "Inflammatory Response", "Allograft Rejection", "IFN-α response", "Complement" and "Apoptosis", among others, being "IFN-γ response" the top-ranked in this category (**Fig. 4f,** grey lanes). The increase of these signalling pathways was more pronounced by αPD1 treatment (**Fig. 4f,** green lanes, see all differentially expressed Hallmarks gene sets in **Extended Fig. 8 c,d**). Of note, these pathways primed by shMDK and exacerbated by ICB are characteristic of acute pro-inflammatory signals[2], which indeed we found enriched in these two transcriptomic profiles (**Extended Fig. 8e**).

The transcriptional changes indicated above raise the potential for clinical implications. There is an acknowledged variability in gene signatures predictive of sensitivity to ICB

(**Supplementary Table 7**). However, IFN-γ is consistently considered as a good response indicator[5,7,48], in part, by activating monocytes/macrophages and promoting $CD8^+$ T cell differentiation[49]. Of note, of the 200 genes annotated as "IFN-γ response" (GO:M5913), we found 117 significantly enriched when MDK is depleted, being further potentiated in the shMDK-αPD1 combination (**Fig. 4g,h**). Moreover, MDK depletion, particularly after αPD1 treatment, increased the expression of a variety of factors associated with the polarization of macrophages to antitumoural phenotypes[50] (**Fig. 4g, h**) and T cell infiltration (**Fig. 4g**). Histological analyses confirmed a significant increase in $CD8^+$ T cells in the shMDK-ICB treated tumours (**Fig. 4i,j**). Together, these data serve as the proof of concept for a combined MDK-immune checkpoint inhibition.

MDK-conditioned macrophages promote T-cell tolerance

To test to which extent macrophages contribute to the suppressive effect of MDK and the response to ICB, treatments were performed using an anti-CSF1R antibody (see **Extended Fig. 9a** for dosing schedule). Treatment with anti-CSF1R (αCSF1R) effectively impaired monocyte accumulation in B16F1-OVA-MDK tumours (**Fig. 5a**), and importantly, it significantly increased the response to αPD1 (**Fig. 5b**; see lack of effects in the MDK-negative counterparts).

To determine whether MDK-educated macrophages compromise T cell function, $CD8^+$ T cell cytotoxicity was analysed using the classical OT-1 transgenic $CD8^+$ T cells specific for the OVA–derived SIINFEKL peptide [46]. As targets, we used B16F10-OVA^{GFP} cells (Control or expressing MDK) to facilitate visualization (see Methods section). As shown in **Fig. 5c**, parental and MDK-expressing melanoma cells were killed similarly well by SIINFEKL-activated OT-1 cells if bone marrow-derived myeloid cells (BMDM) were absent. However, if BMDM were present, MDK-melanoma cells

were more resistant (**Fig. 5c**). This inhibitory activity of MDK on T cell killing required NF-κB signalling in melanoma cells, and Arg1 expression as demonstrated by siRNA against RelA (**Fig. 5d**), and incubation with the Arginase1-specific inhibitor 2(S)-amino-6-boronohexanoic acid (ABH) (**Fig. 5e**).

As activated OT-1 T cells could not kill melanoma cells efficiently in the presence of MDK-educated macrophages, we tested for T cell dysfunction, monitoring key expression of biomarkers for this activity such as PLAUR, HAVCR2 or EOMES[51]. As shown in **Fig. 5f**, we could detect a reproducible increase in mRNA expression of these three genes in OT-1 cells cocultured with MDK-educated BMDM.

Given these results in cultured cells, we then moved to patient data, comparing $MDK^{High\text{-}P}$ vs $MDK^{Low\text{-}P}$ populations of the TCGA dataset (**Fig. 1b,c**). The $MDK^{High\text{-}P}$ patient population was found by GSEA enriched in recently described $CD8^{+}$ dysfunctional/naïve" signature[51] (**Fig. 5g**). We then mined an independently generated "T cell exclusion and dysfunction expression dataset", TIDE, reported in melanoma[11]. Again, the T cell dysfunction signature was enriched in the $MDK^{High\text{-}P}$ melanoma subpopulation (**Fig. 5h**; T cell exclusion did not score in this analysis). Importantly, this MDK-associated TIDE signature was also found enriched in TCGA cohorts of GBM, LUSC and KIRC (**Extended Fig. 9c**), strengthening the relevance of these findings.

MDK correlates with resistance to immune checkpoint blockade in patients

We then leveraged on the finding that the TIDE-T cell dysfunction signature can be exploited to define response to ICB[11]. As summarized in **Fig. 5i**, TIDE classified $MDK^{high\text{-}P}$ melanomas mostly as non-responders, while responders corresponded largely to $MDK^{low\text{-}P}$ profiles (**Fig. 5i**, red and blue respectively). Therefore, we interrogated whether MDK or MDK-associated gene sets correlated to ICB response

in different clinical datasets. We could not find MDK protein staining in melanomas correlating with response to αPD1 antibodies in a series of n=151 metastatic patients (not shown). This was perhaps expected, considering the broad spectrum of transcriptomic and proteomic effects of MDK (**Extended Fig. 5**). Moreover, response to ICB has not been linked to single genes, but rather, to gene networks which, as described by various authors, can be highly heterogeneous[5-9] (see examples of seven signatures for ICB resistance[6,9,11,12,52,53] in **Extended Fig. 9b**). Interestingly, and despite this variability, we found a significant enrichment of genes expressed by the $MDK^{high\text{-}P}$ patient subpopulations in all these seven ICB-resistance signatures (see in red in **Extended Fig. 9b,** with the corresponding NES and FDR q-value).

Next, we assessed MDK-driven transcriptome and ICB in a more direct manner. To this end, we used the RNAseq of bulk B16R2L tumour implants expressing or lacking MDK, and treated with control or αPD1 antibody (**Fig. 4f,g**). In this case, we interrogated five gene signatures reported to define good response to ICB in human patients (see **Supplementary Table 7** gene lists): Signature 1 (Ref[6], αPD1) ; Signature 2 (Ref[7], upregulated genes in responder patients to αPD1); Signature 3 (Ref[48], IFN-γ-related); Signature 4 (Ref[8], αPD1, CTLA4), Signature 5 (Ref[7], upregulated in responders to αPD1+CTLA4). Interestingly, all these gene signatures were found significantly enriched not only in the transcriptome of the B16R2L tumours treated with the shMDK-ICB combination (**Fig. 6a, Extended Fig. 10a**), but also just by depletion of shMDK (**Extended Fig. 10b**). These data, therefore reinforce the priming effect of MDK depletion towards an ICB-responsive expression profile.

Next, we set to narrow down the MDK-associated gene profiles that may be more tightly linked to the response to ICB in human patients. Specifically, we focused on genes deregulated by MDK depletion that were deregulated also by αPD1 (see

Methods). Heatmap in **Fig. 6b** shows the top 100 (out of 245) genes found increased with this approach, and the 17 downregulated counterparts, herein referred to as [shMDK^{up}-ICB^{up}] and [shMDK^{down}-ICB^{down}] genesets, respectively (see **Fig. 6c** for examples, and **Supplementary Table 8** for a complete gene list). Of note, the [shMDK^{up}-ICB^{up}] gene set includes 35 genes previously reported in the ICB and IFN response signatures that we have tested, but also 65 new genes that deserve future attention (**Fig. 6c, Supplementary Table 8**).

The combined [shMDK^{up}-ICB^{up}] and [shMDK^{down}-ICB^{down}] genesets were then used to define an shMDK-ICB score by ssGSEA across six patient cohorts: Cohort 1 (Ref[7]), Cohort 2 (Ref[6]), Cohort 3 (Ref[5]) and Cohort 4 (Ref[53]), treated with αPD1; and Cohort 5 (Ref[54]) and Cohort 6 (Ref[9]), treated with αCTLA4. This shMDK-ICB score was significantly enriched at baseline (pre-treatment) in responder patients of Cohorts 1,2,3,5 and 6, irrespective of αPD1 or αCTLA4 treatment (see examples for overall survival plots in **Fig. 6d** and additional data in **Extended Fig. 10c;** progression-free survival for cohorts with available information for this feature are in **Extended Fig. 10d**). ICB can induce adaptive responses in gene expression profiles[7,52]. Therefore, we tested patient cohorts on-treatment with αPD1 (Cohorts 1[7] and Cohort 2[6]), finding that the responders have significant enrichment of the shMDK-ICB score (**Fig. 6e**). Therefore, these data support a physiologically relevant impact of MDK in controlling genes that define response to ICB.

DISCUSSION

Cancers have long been considered as “wounds that do not heal”, whereby the net balance between pro- vs anti-inflammatory signals determines the potential of malignant cells to proliferate, survive, invade and metastasize[2]. Here, we have

reported the ability of MDK to rewire the transcriptome and proteome of melanoma cells, resulting in an “inflamed”, yet immunosuppressive microenvironment. Mechanistically, we described an autocrine impact of MDK on melanoma cells (driven in part via NF-κB) resulting in a secretome enriched in cytokines (e.g. CSF1, LIF, CCL3 or TGF-β), and chemoattractants (MMP8, SPP1, S100A8/A9 or LGALS1, among others) with no previous links to MDK. This complex secretome was found in turn to exert paracrine effects on macrophages resulting in tolerogenic phenotypes (exemplified by ARG1 expression), leading ultimately to CD8 T-cell dysfunction (see model in **Fig. 6f**). The combination of gain and loss of function analyses in this study demonstrated that MDK is not required just to ensure efficient protumoural signals from NF-κB, but also to suppress an otherwise latent IFN-modulated antitumoural microenvironment (**Fig. 6f**). The relevance of MDK-associated gene expression profiles was illustrated at various levels: (i) separating populations of metastatic melanoma patients with significantly different prognosis, (ii) defining resistance to vaccination in murine systems,(iii) setting the proof of principle for a strategy (based on MDK inhibition) to prime melanoma cells to ICB response, and (iv) revealing yet potential novel targets for therapeutic intervention.

Our data provide insight into different scenarios that contribute to the response to immune checkpoint blockade (ICB) in cancer. While there is an acknowledged variability on the gene signatures being reported, ICB-“cold” tumours are typically defined by a characteristic exclusion of cytotoxic $CD8^+$ T cells[1,10,55-57]. The results here contribute to understanding less defined immune “hot/infiltrated”, but tolerogenic, backgrounds[14,58]. In particular, here we show how $CD8^+$ T cells may acquire a dysfunctional profile via MDK-educated macrophages.

Arguably, one of the most unexpected results of this study is that just removing MDK from melanoma cells was sufficient to reshape macrophages and T cells towards anti-tumoural phenotypes with a markedly induced IFN-signalling profile. This effect on IFN has translational implications, considering that this is one of the most consistent indicators of sensitivity to immune checkpoint blockade (ICB)[5,7,8,48]. The combined use of MDK inhibition with ICB is supported by an enhanced response in our tumour implants in mice, and the identification of 5 (out of 6) cohorts where the shMDK-ICB combined signature was correlated to good responders either to αPD1 or to αCTLA4-based treatments. As immunomodulatory agents may impinge on cross-resistance to targeted therapy[59], our data may have far-reaching implications in patient management.

Of note, while this study focused primarily on metastatic melanoma, we have identified MDK-associated expression profiles with prognostic significance and association to T cell dysfunction in renal cell carcinoma and lung squamous cell carcinoma. Our data also identified T cell dysfunction and suppressive features related to Tregs and TGF-β in glioblastoma, which are of interest to compare to non-canonical effects on CD8+ T cells reported in NF1-associated low-grade gliomas[21]. Moreover, our RNAseq and secretome analyses may serve as a reference to contrast to atherogenesis, neuroinflammation and other autoimmune and degenerative processes, where MDK hyperactivates the immune system[16,18,24,25] instead of acting as an immune suppressor.

In summary, the combination of computational, -omic, histological and functional data in this study provides insight on MDK as a driver of a distinct immune tolerant phenotype. These data not only links MDK signalling to poor prognosis and sets the

proof of principle for dual MDK-ICB inhibition in melanoma, but also serve as a platform for future studies in other tumours and inflammatory diseases.

ONLINE METHODS

Cell culture

The syngeneic mouse melanoma cell lines B16-F1 and B16-F10 are from ATCC (VA, USA), and the highly metastatic B16F1-R2L[61] were provided by M. Detmar, (ETH, Zürich). B16-OVA^{GFP} cells were generated by transfection of a truncated non-secreted ovalbumin (OVA)-GFP fusion protein (bm1 T OVA) were generously supplied by D. Sancho[46]. Human non-metastatic melanoma cells WM164 and metastatic SK-Mel-147 melanoma cells were used as examples of low and high-MDK expression as reported before[15]. RAW264.7 cells were selected as an *in vitro* model of murine macrophages[63]. Glioma cell lines U251, LN18 and T98G were kindly provided by Dr. Massimo Squatrito. All these cells were cultured in Dulbecco's modified Eagle's medium (DMEM, Lonza, cat. no. BE12-604F/U1) supplemented with 10% fetal bovine serum (FBS, Tico, cat. no. A3FBSEU500) and 100 µg/mL Penicillin/Streptomycin (Invitrogen, cat. no. 15070-063). Lung squamous cell carcinoma cell lines A549, H358 and H322M were kindly provided by Dr. Luis Paz-Ares, and cultivated in RPMI cultured medium (GIBCO) supplemented with 10% fetal bovine serum (FBS, Tico, cat. no. A3FBSEU500) and 100 µg/mL Penicillin/Streptomycin (Invitrogen, cat. no. 15070-063). Mouse melanoma cell lines YUMM2.1, YUMM1.1, and YUMMER1.7 were kindly provided by Dr. Marcus W. Bosenberg (Yale, School of Medicine) and were cultured in DMEM-FG12 (1:1) medium, with 10% FBS, 1% NEAA (GIBCO) and 1% Gentamicin (G1264; Sigma-Aldrich). Cells were regularly tested for mycoplasma contamination by

quantitative-PCR. All the melanoma cell lines were authenticated using GenePrint 10 Loci Service.

Primary mouse and human macrophages

Murine bone marrow-derived macrophages (BMDM) were obtained from the femurs of healthy C57BL/6J mice and maturated with murine MCSF (10 ng/ml, Peprotech), or GM-CSF (10 ng/ml, Peprotech) and IL-6 (10 ng/ml, Peprotech) in 10% gelatin-coated petri dishes, for up to 5 days. When indicated, BMDM were additionally differentiated in the presence of conditioned medium from WM164-MDK or B16-MDK melanoma cells or their isogenic controls (transduced with control empty lentiviruses)[15].

Human macrophages were prepared from frozen plateletpheresis containing an enriched population of monocytes (~10^7 million monocytes per vial). Vials were thawed and seeded with 1 ml of adhesion media containing L-glutamine-enriched RPMI (Thermo Fisher Scientific), supplemented with gentamycin (1%) and 5% human AB serum (Sigma-Aldrich) heat-inactivated at 56°C for 30 mins. Cells were plated into 6-well cell culture dishes at a concentration of 1x10^6 monocytes/well and incubated at 37°C and 5% CO_2. The supernatant was removed 2 hours later and replaced with differentiation media (adhesion media supplemented with 5% pooled human AB serum, and 20 ng/ml human MCSF). Media was replaced on day 3 and day 6 post-isolation with adhesion media. Human monocyte-derived macrophages (HMDMs) were treated on day 7 with conditioned medium from shCtrl or shMDK isogenic derivatives of SK-Mel-147. Samples and data from patients included in this study were provided by the Biobanco Hospital Universitario Puerta De Hierro Majadahonda (Huphm) / Instituto De Investigación Sanitaria Puerta De Hierro-Segovia De Arana (IDIPHISA) (PT17/0015/0020 in the Spanish National Biobanks Network), they were

processed following standard operating procedures with the appropriate approval of the Ethics and Scientific Committees.

Mouse models and human samples.

C57BL/6JOlaHsd mice were from Harlan. Crl:NU(Ico)-*Foxn1*^{nu} Swiss Nude mice were obtained from Charles River. B6.*Ptprc*^{a}*Rag1*$^{ko/ko}$Tg(TcraTcrb)1100Mjb/J (OT-I mice) were kindly provided by D. Sancho (CNIC, Madrid) for isolation of OT-I T cells. Mouse xenografts were generated in 8-week old C57BL/6 mice by subcutaneous implantation of 0.5 x 10^6 cells (one injection site per mouse. Animals were randomized in groups for analyses/collection. No blinding was done in the analysis of tumour xenografts. Tumour growth was followed every two days by measuring the two orthogonal external diameters using a calliper. Tumour volume was calculated as V = π/6 x L x W x H, where L, W and H represent length, width and height, respectively. Tumours were excised and processed for histological analysis when they reached 1 cm^3. All experiments with mice were performed in accordance with protocols approved by the Institutional Ethics Committee of the CNIO and the Instituto de Salud Carlos III. Human tumour biopsies were obtained from University Hospital Zurich or Hospital 12 Octubre (Madrid), with the corresponding ethical protocols approved by their Clinical Investigation Ethical Committees.

Treatments

Human recombinant MDK (Peprotech, Rocky Hill, NJ) was used at 10 ng/ml concentration. Pharmacological inhibition of NF-kB was performed using an IKK2 inhibitor (TPCA-1, Selleckchem) at 1μM. Pharmacological inhibition of Arg1 was performed using an Arginase1-specific inhibitor 2(S)-amino-6-boronohexanoic acid (ABH; Sigma Aldrich, 500nM). αPDL1 blocking antibody (clone B7-H1, BioXcell) or its IgG2b control isotype (Clone LTF-2, BioXcell) and αPD1 blocking antibody (clone

RMP-14, BioXcell), with its IgG2a control isotype (Clone 2A3, BioXcell) were administered intraperitoneally every three days at a dose concentration of 10 mg/Kg body weight. The inhibition of MDK *in vivo* was performed by intraperitoneal administration of the small molecule 3-[2-(4-Fluoro-benzyl)imidazo[2,1-b][1,3]thiazol-6-yl]-2H-chromen-2-one (MDKi, Calbiochem, 9 mg/Kg BW) for 5 consecutive days. Ultra-LEAF™ Purified anti-human S100A8/A9 Heterodimer Antibody (Anti-Calprotectin blocking antibody) (Clone A15105B, Biolegend) was added to the conditioned medium at a concentration of 1 μg/ml, and incubated at 37ºC for 1h, before using this conditioned medium for functional assays.

Gene silencing and overexpression by lentiviral transduction.

MDK silencing was performed by lentiviral-driven expression of shRNAs, with pLKO-constructs purchased from Sigma (St. Louis, MO) as previously reported[15]. For human cell we used, MDK-sh5 (NM_002391.3-621s21c1) and for mouse, MDK-sh5 (NM_010784.4-734s1c1). Non-Target shRNA (CAACAAGATGAAGAGCACCAA) was used as control. Viral production in 293FT cells and infections were performed as previously described[15,63]. Infected cells were selected by incubation with puromycin (1μg/mL) and MDK downregulation was determined by protein immunoblotting, ELISA or qRT-PCR (see below). For RelA (p65) silencing, Lipofectamine RNAiMAX Transfection was used to transduce siRNA for human RELA (HSS109161, Thermofisher, MA) or its mouse counterpart (MSS208588, Thermofisher), in the corresponding cell lines, having an unspecific siRNA (12935-200, Thermofisher) as control.

For the overexpression of human MDK, ORF lentiviral expression vector pReceiver-Lv105-A0792 (MDK) and the corresponding empty vector were purchased from Genecopoeia (Rockville, MD).

Quantification of MDK secretion

Cells were incubated for 24h in DMEM-10% FBS before collection and MDK secretion was estimated by ELISA (Peprotech, 900-K190) following manufacturer's instructions[15].

Transcriptomic and proteomic (LC-MS/MS) analyses.

Transcriptomic analyses were performed in gain and loss-of-function settings (GOF and LOF) generated in isogenic cell pairs as described before[15]: (i) WM164 control and WM164-overexpressing MDK (GOF), in (ii) SK-Mel-147 expressing shC or shMDK (LOF). Three biological replicates were performed for these analyses. Additionally, we tested implants of B16R2L melanoma cell lines expressing shC or shMDK and treated with anti-PD1 or IgG2a control (10 mg/Kg, three times per week), with four biological replicates. Fifty-base-pair single-end sequenced reads were analysed with the nextpresso pipeline[64] as follows: sequencing quality was checked with FastQC v0.11.0. Reads were aligned to the human genome (GRCh37/hg19) with TopHat-2.0.10 using Bowtie 1.0.0 and Samtools 0.1.19, allowing 2 mismatches and 20 multihits. The UCSC hg19 gene annotation from https://ccb.jhu.edu/software/tophat/igenomes.shtml was used. Transcript quantification and differential expression were calculated with Cufflinks 2.2.1. The differential expression profile was analysed using limma (R, package).

Regarding RNAseq in the B16R2L specimens, 500 ng of Total RNA samples were used. Sample RNA Integrity numbers were 8.6 on average (range 5.8-9.2) when assayed on an Agilent 2100 Bioanalyzer. Sequencing libraries were prepared with the "QuantSeq 3‘ mRNA-Seq Library Prep Kit (FWD) for Illumina" (Lexogen, Cat.No. 015) by following manufacturer instructions. cDNA libraries are purified, applied to an Illumina flow cell for cluster generation and sequenced on an Illumina NextSeq 550

(with v2.5 reagent kits) by following manufacturer's protocols. Eighty five-base-pair single-end sequenced reads followed adapter and polyA tail removal as indicated by Lexogen. The resulting reads were analysed with the nextpresso pipeline as follows: sequencing quality was checked with FastQC v0.11.0. Reads were aligned to the mouse genome (GRCm38/mm10) with TopHat-2.0.10 using Bowtie 1.0.0 and Samtools 0.1.19, allowing 3 mismatches and 20 multihits. The Gencode vM20 gene annotation for GRCm38 was used. Read counts were obtained with HTSeq. Differential expression and normalization were performed with DESeq2, filtering out those genes where the normalized count value was lower than 2 in more than 50% of the samples.

For secretome profiling, media was collected from $6x10^6$ cells of the indicated cell populations 24h after plating in completed DMEM medium. Proteins were digested by means of the standard FASP (Filter Aided Sample Preparation) protocol[65]. Briefly, samples were resuspended in UT buffer (8M urea in 100 mM Tris-HCl, pH=8.01). Proteins were then reduced with 10 mM DTT, alkylated using 50 mM IAA for 20 min in the dark. Proteins were digested with Lys-C (Wako, Neuss, Germany) during 6 h (1:50 enzyme:protein ratio). Finally, samples were diluted in 50 mM ammonium bicarbonate to reduce the urea concentration to 1M, and were subsequently digested with trypsin (Promega, Madison, WI; 1:100 sample concentration, overnight at 37 °C). Resulting peptides were desalted and using micro-columns filled with Poros Oligo R3 beads (Life Technologies). Samples were dried and dissolved in 30 µL of 0.1% formic acid (FA). Peptides were separated by RP chromatography using a nanoLC Ultra system (Eksigent, Dublin, CA), directly coupled with a LTQ-Orbitrap Velos instrument (Thermo) via nanoESI (ProxeonBiosystem, Waltham, MA). Peptides were loaded onto a Reprosil-Pur C18 column (3 μm, 400 x 0.075 mm; Dr. Maisch, Ammerbuch-Entringen

Germany), with a trapping column (Prot Trap Column 0.3 x 10 mm, ReproSil C18-AQ, 5 µm), for 10 min with a flow rate of 2.5 µL/min of loading buffer (0.1% FA). Elution was performed with a 120 min linear gradient (buffer A: 2% ACN, 0.1%FA; buffer B: 100% ACN, 0.1%FA) at 300 nL/min. Peptides were directly electrosprayed into the mass spectrometer using a PicoTip emitter (360/20 OD/ID µm tip ID 10 µm, New Objective) at 1.4 kV spray voltage with a heated capillary temperature of 325°C and S-Lens of 60%. Mass spectra were acquired in a data-dependent manner, with an automatic switch between MS and MS/MS scans using a top 10 method. MS spectra were acquired with a resolution of 60000 (FWHM) at 400 m/z in the Orbitrap, scanning a mass range between 350 and 1500 *m*/*z*. Peptide fragmentation was performed using collision-induced dissociation (CID), set at 35%. Label-free quantification was performed in MaxQuant (1.5.3.30) using default settings and further statistical analysis of the quantitative data was conducted with Perseus (1.5.5.2).

Bioinformatic analyses, ssGSEA and score generation.

Single-cell RNA-seq data was extracted from GSE72056 (ref[10]), comprising 4645 cells from 19 melanoma patients, using the provided normalization and cell labels. To visualize the clusters of different cells, the UMAP (Uniform Manifold Approximation and Projection) dimensionality reduction algorithm was applied, following PCA (Principal component analysis) to embed each cell in a two-dimensional plot. Enrichment Scores of the GOF and LOF expression profile in each cell were computed with single-sample Gene Set Enrichment Analysis (ssGSEA), as implemented via gseapy. To improve visualization, the Enrichment Scores for each cell were further ranked by percentile to form Enrichment Score Ranks ranging from 0 to 1. Accordingly, differences between

Enrichment Score Ranks among cellular populations were assessed through the two-tailed Mann-Whitney U test.

mRNA profiles extracted from GOF and LOF experiments performed in melanoma cell lines were used for ssGSEA to define a MDK-enrichment score in biopsies of metastatic melanomas in TCGA. TCGA data was downloaded using firebrowse (https://www.firebrowse.org). The MDK-enrichment score was generated using GSVA[66] (R package) with ssGSEA as an enrichment method. The MDK-enrichment score was calculated as the difference between up- and down-regulated genes of the GoF with respect to those also up and downregulated by LOF independently. Thus, each patient is represented by the difference of the ssGSEA score of the GOF and LOF, respectively. No overlap between the upregulated and downregulated genes was allowed. The MDK-enrichment score per patient (related to GOF and LOF) was tested for P-value distribution. To this end, 10,000 linear models with geneset permutation were performed to create a P-value null distribution, Pearson correlation and R-squared. No linear model was found, having a more extreme adjusted P-value than the obtained with the GOF and LOF mRNA transcriptome. TCGA melanoma samples whose mRNA expression profiles scored above or below the 15th percentile (herein referred to as MDK$^{high\text{-}P}$ and MDK$^{low\text{-}P}$, respectively) were selected for subsequent identification of enriched signaling cascades, immune profiling and analysis of prognostic significance. This cut off was selected as it allowed for a sizable number of biopsies (MDK$^{High\text{-}P}$, n=42; MDK$^{low\text{-}P}$, n=30) to represent patients most enriched in the mRNA transcriptome of MDK-GOF and LOF settings. The differential expression profiles between MDK$^{high\text{-}P}$ and MDK$^{low\text{-}P}$ patients were analyzed using limma (R, package). Gene set collections were retrieved from annotations by the Broad Insitute Library of Molecular Signature Databases (MSigDB), including Reactome, KEGG, PID,

BIOCARTA and Hallmarks pathway databases. GSEA tests were tested for false discovery rate (FDR q-value). After Kolmogorov-Smirnov correction for multiple testing, only those pathways with FDR q-value <0.25 were considered as significant Immune score comparison was performed using precalculated RNA-Seq-V2 scores from ESTIMATE and reported data in Ref[32]. For **Fig. 1c-d**, significant genesets were manually grouped in the indicated biological processes.

For geneset selection in B16R2L-associate gene expression profiles, we first selected genes differentially deregulated by MDK depletion (FDR<0.05), comparing RNAseq data of shMDK-IgG2a vs shC-IgG2a. Within these genes, we then subselected those induced by αPD1 in a significant manner (FDR<0.05), namely, in shMDK-PD1 vs shC-PD1. The selected genes were then ranked as follows: (shMDK-PD1 vs shC-PD1)/ (shMDK-IgG2a vs shC-IgG2a). This approach revealed 245 genes differentially expressed by MDK depletion and ICB treatment. Top 100 of these genes were selected as the [shMDK^{up}-ICB^{up}] gene set. The 17 genes significantly downregulated both in shMDK-IgG2a vs shCtrl-IgG2a and shMDK-PD1 vs shCtrl-PD1 (FDR < 0.05) were selected to compose the shMDK^{down}-ICB^{down} geneset. For analyses of overall survival and progression-free survival in ICB-treated patients, we estimated the enrichment of the [shMDK^{up}-ICB^{up}] gene sets and the corresponding ones for [shMDK^{down}-ICB^{down}] per patient, using the GSVA[66] (R package) with ssGSEA as enrichment method. The shMDK-ICB score was estimated as [shMDK^{up}-ICB^{up}] minus [shMDK^{down}-ICB^{down}] score before normalization. Patients whose mRNA expression profiles were within the up or lower 25th percentile of shMDK-ICB scores were compared for their overall survival and progression-free survival and plotted in standard Kaplan Meier curves. Statistics: Log-rank (Mantel-Cox) test. Controls for random bias were also performed

for 10,000 randomly generated genesets of the equivalent sample size (*n* = 117). No significant correlations to treatment response were found (data not shown).

To follow is a summary of the different nomenclature of expression profiles and scores used in this study:

MDK-GOF and MDK-LOF **gene profiles**. Genesets that are differentially deregulated by MDK expression or depletion in melanoma cell lines, respectively.

MDK^{GOF} or MDK^{LOF} **score**. Value obtained for a given transcriptome (i.e. for each patient in a TCGA cohort) by ssGSEA. Specifically, these scores reflect the extent to which a given transcriptomic profile is enriched for the GOF or LOF-gene sets of the melanoma cell lines. No overlap between the GOF or LOF-profiles was allowed for this analysis.

$MDK^{High\text{-}p}$ or $MDK^{Low\text{-}p}$ **patient populations**. Patient subgroups (from the TCGA dataset) within the top or bottom 15th percentiles of MDK^{GOF} and MDK^{LOF} scores. These are the patients that more closely recapitulate the effect of MDK overexpression or depletion, respectively.

shMDK-ICB **geneset**. Genes found significantly upregulated or downregulated in xenografts depleted for MDK and treated with immune checkpoint blockade (αPD1 antibody). In the manuscript we focused on the [$shMDK^{up}$-ICB^{up}] set (top 100 upregulated in both conditions) and the downregulated ones [$shMDK^{down}$-ICB^{down}].

shMDK-ICB **score**. Enrichment value for the shMDK-ICB **geneset** obtained by ssGSEA in 6 published cohorts of ICB treated melanoma patients.

Heatmap and correlation graphs for RNA and protein levels were created by Perseus v1.5.1.6, or Morpheus Heatmaps (https://software.broadinstitute.org/morpheus), using a Log2 normalization. Protein networks were created by Search Tool for the Retrieval of Interacting Genes/Proteins (STRING), and Venn diagrams were created by using online tools Venny v2.0.

Histological analyses

Tissues were fixed in formalin and embedded in paraffin. Sections were prepared for hematoxylin-and-eosin (H&E) staining. For immunostaining, 3 µm-thick paraffin sections were deparaffinized and antigen retrieval was performed using Tris-EDTA pH 9. Endogenous peroxidase activity was quenched with 3% hydrogen peroxide. Ultravision ONE Detection System (RTU, Thermo Scientific, Waltham, MA) was used following the manufacturer's protocols. Sections were counterstained with hematoxylin (Anatech, Battle Creek, MI) and mounted with permanent mounting medium. For immunofluorescence, tissue sections were deparaffinized, incubated overnight with primary antibodies at 4 °C in a humidified chamber and then rinsed and incubated with fluorescent secondary antibodies for 1 hour at room temperature. Nuclei were counterstained with DAPI (4´,6-diamidino-2-phenylindole; D9542; Sigma-Aldrich). Negative controls were obtained by omitting the primary antibody. Image mosaics were acquired at 40xHCX PL APO 1.2 N.A. oil immersion objective using a confocal TCS-SP5 (AOBS-UV) confocal microscope and "intelligent matrix screening remote control" (iMSRC) tool. Images were subsequently analysed with ImageJ software. The following antibodies were used at the indicated dilutions: Arg1 1:400 (Santa Cruz sc-1835), MDK 1:50 (Santa Cruz sc-46701), YM1 1:200 (AF2446, R&D Systems); CD8a (94A, CNIO Monoclonal Antibody Core Unit) and iNOS 1:100 (610333, BD Biosciences). Multivariate analyses of MDK expression with respect to patient age and features of ulceration and macrophage staining (CD163 marker) were performed with a cumulative link mixed model fitted with the clmm2 function in package ordinal, using the adaptive Gauss-Hermite quadrature approximation with 10 quadrature points. P values are based on the Wald statistic. The performance of the best ordinal regression model was being assessed using a backward selection procedure and the likelihood ratio chi-square statistic.

Ovalbumin-based vaccination (immunization)

The procedure for mice immunization with the OVA protein is summarized in **Extended Fig. 7a**. Mice received Complete Freund's Adjuvant (CFA) emulsion as a negative control or 10 µg of chicken ovalbumin (OVA, grade IV, Sigma) emulsified with CFA, in two subcutaneous (s.c) injections of 25 µl per foreleg. Ten days later, B16-F10 OVA^{GFP} tumour cells (5×10^5 in 100 µl of PBS) were inoculated in C57BL/6 mice by subcutaneous injection. A vaccine boost was performed on day 15 by two s.c. injections per foreleg (25 µl) of 10 µg lipopolysaccharide (LPS) as a negative control, or 10 µg LPS plus 10 µg OVA (grade IV, Sigma; MI, USA). On day 21 post-immunization, mice were euthanized and their serum analyzed by ELISA using Anti-Ovalbumin IgG1 (mouse) ELISA Kit (Cayman Chemicals; 500830).

In vivo monocyte/macrophage depletion assay

To deplete macrophages in mouse models, animals were pre-treated for 2 weeks with 400 µg αCSF1R (clone AFS98, BioXCell BE0213) or the corresponding IgG2a isotype control (2A3; BioXCell BE0089), administered intraperitoneally at alternative days three times per week. Two weeks after these treatments, tumours were engrafted subcutaneously with the indicated melanoma cell line populations. αCSF1R depletion was sustained thereafter, and animals were treated with control or αPD1 antibody as described in **Extended Fig. 9a**.

RNA extraction and qRT-PCR

Total RNA was extracted and purified from cell pellets using RNeasy Mini-Kit (QIAGEN) following the manufacturer's instructions. RNA concentration was determined by NanoDrop Spectrophotometer ND-100 (NanoDrop Biotechnologies). Total RNA (1-2 µg) was retro-transcribed into cDNA using the High capacity cDNA

reverse transcriptase kit (Applied Biosystems), according to the manufacturer´s protocol. Twenty ng of the total cDNA were subjected to real-time quantitative polymerase chain reaction (RT-qPCR at 60°C annealing temperature) using Power SYBR® Green PCR Master Mix (Applied Biosystems). Assays were performed in triplicates on the QuantStudio™ 6 Flex Real-Time PCR System (Applied Biosystems). The forward (FW) and reverse (RV) primer sequences were the following:

hS100A9 (FW) 5'-GTGCGAAAAGATCTGCAAAA, hS100A9 (RV) 5'-TCAGCTGCTTGTCTGCATTT

hCCL3 (FW) 5'-CAGAATCATGCAGGTCTCCAC, hCCL3 (RV) 5'-GCGTGTCAGCAGCAAGTG

hCCL2 (FW) 5'-AGTCTCTGCCGCCCTTCT, hCCL2 (RV) 5'-GTGACTGGGGCATTGATTG

hTNF (FW) 5'-CGAGTGACAAGCCTGTAGC, hTNF (RV) 5'-GGTGTGGGTGAGGAGCACAT

hFOSL1 (FW) 5'-CGAAGGCCTTGTGAACAGA, hFOSL1 (RV) 5'-GTTCCT TCCTCCGGTTCCT

hLIF (FW) 5'-TGAAGTGCAGCCCATAATGA, hLIF (RV) 5'-TTCCAGTGCAGAACCAACAG

hIL6 (FW) 5'-CCAGGAGCCCAGCTATGAAC, hIL6 (RV) 5'-CCCAGGGAGAAGGCAACTG

hIL1B (FW) 5'-TACCTGTCCTGCGTGTTGAA, hIL1B (RV) 5'-TCTTTGGGTAATTTTTGGGATCT

hTGFB1 (FW) 5'- CCCTGGACACCAACTATTGC, hTGFB1 (RV) 5'-CTTCCAGCCGAGGTCCTT,

hLGALS1 (FW) 5'-CGCCAGCAACCTGAATCT, hLGALS1 (RV) 5'-CAGGTTCAGCACGAAGCTCT,

hRELA (FW) 5'- CAGGCGAGAGGAGCACAGA, hRELA (RV) 5'-TGTGTAGCCATTGATCTTGATGGT,

hCXCL16 (FW) 5'- GCCCTTTCCTATGTGCTGTG, hCXCL16 (RV) 5'-CAGGTATATAATGAACCGGCAGAT,

hRELT (FW) 5'- AGCCGTACAAAGTGGCTGAA, hRELT (RV) 5'-CTCACTTAGCCGGACCACAT,

hCSF1 (FW) 5'-AGTCCGAGGGATCCTCCA, hCSF1 (RV) 5'-CGCTCTCTGAGGCTCTTGAT,

hWNT5A (FW) 5'- GCACTGTGGATAACACCTCTG, hWNT5A (RV) 5'-CGCGTATGTGAAGGCCGTC,

hS100A6 (FW) 5'-ACTGCGACACAGCCCATC, hS100A6 (RV) 5'-GAAGATGGCCACGAGGAG,

hMDK (FW) 5'-CCTGCAACTGGAAGAAGGAG, hMDK (RV) 5'-CTGGCACTGAGCATTGTAGC,

mArg1 (FW) 5'- GGAATCTGCATGGGCAACCTGTGT, mArg1 (RV) 5'-AGGGTCTACGTCTCGCAAGCCA,

mCcl7 (FW) 5'-TTCTGTGCCTGCTGCTCATA, mCcl7 (RV) 5'-TTGACATAGCAGCATGTGGAT,

mNos2 (FW) 5'-GTTCTCAGCCCAACAATACAAGA, mNos2 (RV) 5'-GTGGACGGGTCGATGTCAC,

mTnf (FW) 5'- AGGGATGAGAAGTTCCCAAATG, mTnf (RV) 5'- GCTTGTCACTCGAATTTTGAGAAG,

mIl10 (FW) 5'-TAAGGCTGGCCACACTTGAG, mIl10 (RV) 5'-GTTTTCAGGGATGAAGCGGC,

mCcl2 (FW) 5'-CATCCACGTGTTGGCTCA,

mCcl2 (RV) 5'-GATCATCTTGCTGGTGAATGAGT, mCd274 (FW) 5'- AAATCGTGGTCCCCAAGC,

mCd274 (RV) 5'- TCCTCATGTTTTGGGAACTATCT, mPlaur (FW) 5'-GTGTTGCAACTACACCCACTG, mPlaur (RV) 5'- ATTCGGTGGAAAGCTCTGAA, mHavcr2 (FW) 5'-TTTTCAGGTCTTACCCTCAACTG, mHavcr2 (RV) 5'- CATAAGCATTTTCCAATGACCTT, mEomes (FW) 5'- CCCTATGGCTCAAATTCCAC, mEomes (RV) 5'- AAGCTCAAGAAAGGAAACATGC,

18s (FW) 5'-TTGGAGGGCAAGTCTGGTG, 18s (RV) 5'- CCGCTCCCAAGATCCAACTA,

HPRT (FW) 5'-CCTGGCGTCGTGATTAGTGAT, HPRT (RV) 5'-AGACGTTCAGTCCTGTCCATAA.

Protein immunoblotting

Cell lysates were prepared in RIPA buffer supplemented with proteinase/phosphatase inhibitor essentially as previously described[15]. Protein concentrations were determined using the Bio-Rad Protein Assay (Bio-Rad Laboratories). Total cell lysates were subjected to electrophoresis in 10, 12 or 4-20% polyacrylamide gradient SDS gels under reducing conditions, and subsequently transferred to Immobilon-P membranes (Millipore, Bedford, MA, USA) using Mini Trans-Blot Cell system (Bio-Rad Laboratories). Transfer was performed at 100 V for 1.5 hours at 4 °C. Membranes were blocked and were incubated overnight at 4 ºC with the corresponding primary antibody according to the specifications of the manufacturer. The following primary antibodies were used: from Santa Cruz Biotechnology, ARG1 1:2500 (sc-18354) and

p65 1:1000 (sc-372); from Cell Signaling Technology phospho-p65 ser536 1:500 (3033) and from Sigma-Aldrich, β-Actin 1:5000 (A5441) and Vinculin 1:500 (V9131). The HRP-conjugated secondary antibodies used were anti-mouse and anti-rabbit (GE Healthcare) or anti-goat (Jackson Immunoresearch). Protein bands were detected by the ECL system (GE Healthcare, Buckinghamshire, UK).

T cell Cytotoxicity assay

B16F10-OVA^{GFP}-MDK or isogenic Control ($4x10^5$) were seeded in 24-well culture dishes for 24h. BMDM (prepared as indicated before) were then seeded on top of these B16F10-OVA^{GFP} cell populations at a 1:2 ratio in RMPI medium + glutamine (Gibco, cat. no. A14517-01) containing 10% of heat-inactivated Fetal Bovine Serum (FBS, Lonza, cat. no. DE14-801F), 100 µg/mL Penicillin/Streptomycin (Invitrogen, cat. no. 15070-063, 200nM Glutamine, 1% non-essential amino acids (MEM amino acids, Gibco, cat. no. 11130-036), 1% sodium pyruvate (Gibco, cat. no. 11360070), and 0.01% β-Mercaptoethanol (Gibco, cat. no. 31350-010). After 24h, $5x10^5$ SIINFEKL-activated OT-1 T effector cells were then added to the culture for an additional 24 hours. Cells were trypsinized and stained for CD8 (53-6.7, Biolegend) as described below, and analyzed by flow cytometry. Cell death was determined by DAPI expression in GFP positive cells.

Immune profiling by flow cytometry

Implants of the indicated melanoma cell populations were dissected from mice at ~500 mm^3 and measured for total weight. Biopsies were then minced using scalpels and digested with 500 U/ml Collagenase IV (Sigma), and 200 mg/ml DNAse I (Roche) per 0.3 grams of tumour weight for 30 min at 37 °C. After incubation, cell suspensions were then passed through a 40 µm cell strainer to remove large pieces of undigested tissue. Erythrocytes were lysed using Red Blood Cell Lysis Solution (Qiagen, 79217).

For cell surface staining, $1x10^6$ cells were incubated with anti-Fc receptor blocking antibody (clone 2.4G2) and stained with indicated antibodies in DPBS, 2% BSA and 5 mM EDTA, for 30 min on ice. Viability was assessed by staining with DAPI. FoxP3 staining was performed using FoxP3/Transcription Factor Staining Buffer Set (eBioscience) following the manufacturer's instructions. For intracellular staining of Arg1, cells were first fixed and permeabilized using Fixation/Permeabilization Solution Kit (BD, 554714). LIVE/DEAD® Fixable Aqua Dead Cell Stain Kit (ThermoFisher Scientific) was used to assess the viability staining of fixed cells. All flow cytometry was performed on a BD Fortessa flow cytometer. Analysis of flow cytometry data was done using Flowjo (Treestar). Flow cytometry antibodies were used as follows: CD45-Pe-TexasRed (I3/2.3) was from Abcam; NK1.1-BUV421 (PK136), CD4-PE (RM4-5) and CD8-FITC (53-6.7), were from BD Bioscience; CD11b-PerCPCy5.5 (M1/70), CD4-PeCy7 (RM4-5), CD45-APC (30-F11),Ly6C-PE (AL-21), CD11c-BUV737 (HL3), CD8a-FITC (53-6.7), Ly6C-FITC (AL-21) and Ly6G-PeCy7 (1.A8) were from BD Pharmigen, CD3-APC-Cy7 (17A2), CD45-APC-Cy7 (30-F11), I-A/I-E AF700 (MHCII, clone M5/114.15.2), CD103-BV421 (2E7), and F4/80-AF647 (BM8) were from Biolegend, CD25-PerCPCy5.5 (PC61.5), F4/80-APCeF780 (BM8) and FoxP3-PE (FJK-16s) were from eBioscience, and ARG1-APC (P05089) was purchased from R&D systems.

Cells were discriminated using the following combinations of cell markers after gating on single cells (discriminated by FSC-A and FSC-W) and excluding non-viable cells by staining with DAPI or LIVE/DEAD® Fixable Aqua Dead Cell Stain Kit and excluding debris with SSC-A and FSC-A (see representative gating strategies in **Extended Fig. 3e-g**):

CD4+ Th cells: $CD45^+CD3^+CD4^+CD8^-$ $FoxP3^-$

CD8+ Tcyto cells: $CD45^+CD3^+CD4^-CD8^+$

Treg: $CD45^+CD3^+CD4^+$ $CD8^-FoxP3^+CD25^+$

TAMs: $CD45^+CD11b^+Ly6G^-F4/80^+$

Monocytes: $CD45^+CD11b^+Ly6C^+Ly6G^-$

Neutrophils: $CD45^+CD11b^+Ly6G^+Ly6C^-$

NKT cells= $CD45^+CD3^+NK1\text{-}1^+$

NK cells= $CD45^+CD3^-NK1\text{-}1^+$

DC1= $CD45^+CD11b^+CD11c^+MHCII^+CD24^+CD103^+$

DC2= $CD45^+CD11b^+CD11c^+MHCII^+CD24^+CD103^-F4/80^-$

NF-κB reporter assay.

To assess for NF-κB activity we used a NF-κB reporter plasmid obtained from Addgene (Addgene Plasmid #106979), which contains five copies of NF-κB binding sites cloned into psiCHECK2 (Promega) to drive the expression of Firefly luciferase (hluc+). This plasmid includes a Renilla luciferase as a transfection control. Cells from the indicated populations were seeded in 96-well plates and transfected with 0.25 µg of the reporter plasmid using Lipofectamine 3000 (Invitrogen). Cells were cultured for an additional 24h with DMEM without FBS. Cells were then lysed, and luciferase activity was measured using the Dual Glo-Luciferase assay system (Promega, PF-E2920). The Firefly luciferase activity was normalized to the Renilla luciferase activity. Six independent repeats were performed.

Data Availability

The WM164-GOF and SK-Mel-147 LOF RNAseq data have been uploaded to the Gene Expression Omnibus (GEO) repository with the dataset identifier GSE131203. The identifier for B16R2L RNAseq is GSE150401. Mass spectrometry proteomics data

were deposited to the ProteomeXchange Consortium via the PRIDE partner repository with the dataset identifier PXD013843.

Statistics and Reproducibility Tumour growth curves were analysed by one way and two-way ANOVA with Dunnett´s multiple comparison test (mixed model) considering matching among the measures at different time points. P-values or adjusted P-values were indicated in each figure for statistically significant comparisons ($P<0.05$). For the analysis of proteomic data, relative label-free quantification (LFQ) values were log_2 transformed and missing data were imputed based on the observed normal distributions (width value = 0.3 and down-shift = 1.8). Then, two-tailed Student's Test was performed with an FDR <0.01 in the Perseus software. For other techniques and procedures, statistical tests are indicated in the corresponding figure legends. For simplicity, figures only show significant P-values.

For **Figure 2a**, seven representative pictures were taken of tumors from three biological replicates from each condition. One of each tumor (WM164-NEG and WM164-MDK) was selected for whole-sample scan. For **Extended Figure 3a,b**, ten pictures were taken, of three biological replicas per condition. For **Extended Figure 7b**, eight pictures were taken, of three biological replicas per condition.

Full immunoblots are included in the Supplemental Figure 1. Excel files for the different figure panels were uploaded to the online Source Data section of the manuscript.

ACKNOWLEDGEMENTS

The authors thank the colleagues at the CNIO Melanoma Group, as well as at the laboratories of Hector Peinado and Manuel Valiente (CNIO) for help and support. Isabel Blanco, Soraya Ruiz, Virginia Granda, Sheila Rueda (CNIO), the animal Facility, Histopathological Unit, Confocal Microscopy Unit and Crystallography & Protein Engineering Unit of CNIO for assistance with the mouse colonies and histopathological and protein analyses; David Sancho (CNIC; Madrid Spain) for B16-OVA^{GFP} cells and the OT-I mice strain and for scientific guidance. Patrick Turko (Univ. Zurich) provided advice on the statistical analyses of tissue microarrays. The authors wish to thank also the donors, and the Biobank Hospital Universitario Puerta De Hierro Majadahonda (HUPHM) / Instituto De Investigación Sanitaria Puerta De Hierro-Segovia De Arana (IDIPHISA) (PT17/0015/0020 in the Spanish National Biobanks Network) for the human specimens used in this study. M.S.S. is funded by grants from the Spanish Ministry of Economy and Innovation (SAF2017-89533-R), Team Science and Established Investigator Awards by the Melanoma Research Alliance, and by grants from the Worldwide Cancer Research and Fundación “La Caixa”**.** M.S.S., P.-OR and J.-RP are funded by a collaborative grant from Asociación Española Contra el Cáncer (AECC). D.O. is funded by grants from the Spanish Ministry of Health (AES-PIS PI18/1057) and “Beca Leonardo a Investigadores y Creadores Culturales 2018 de la Fundación BBVA”. D.C-W was a recipient of a predoctoral fellowship from “Fundación La Caixa” and is currently funded by the AECC. The CNIO Proteomics Unit belongs to ProteoRed, PRB2-ISCIII, supported by grant PT13/0001. N.I. and J.M. are funded by SAF2013-45504-R (MINECO). J.M. is also supported by Ramon y Cajal Programme (MINECO) RYC-2012-10651. M.C-A. and X.C. were funded by the Immutrain Marie

Skłodowska-Curie ITN Grant. S.H. received funding from the European Union's Horizon 2020 research and innovation programme under grant agreement No 641458.

AUTHOR CONTRIBUTIONS

M.S.S., D.O., and D.C-W conceived and designed expression studies and mechanistic analyses in this work. D.C-W developed the protocols to define MDK-induced immunophenotyping in vivo, performed the histological assessment of MDK and other immune markers, characterized MDK effects in human and mouse cell lines. D.C-W and D.O performed *in vivo* αPD1 and αPDL1 treatments in all settings (i.e. MDKi, αCSFR1), human histological validations, and contributed to the proteomic and transcriptomic data analyses. D.O overexpressed and depleted MDK, performed the proteomic and transcriptomic analyses of the melanoma cell lines, the computational characterization of MDK-associated gene expression and ICB responses, and coordinated additional bioinformatic analyses. M.P.L, S.H, J.L.R.P, P.O and P.K. provided paraffin-embedded specimens for pathological analyses of MDK expression in human specimens, coordinated and interpreted the univariate and multivariate estimations of MDK-associated correlations to macrophage markers. M.C-A. helped with the validation of MDK effect in melanoma cells *in vitro,* flow cytometry and histological analysis, and contributed to the animal experiments. X.C. contributed to the animal experiments and flow cytometry analysis, and prepared cell lines for *in vitro* experiments with other cancer cell lines and OVA models. P.C.P helped with the *in vitro* experiments and human histological quantifications. K.T performed the ssGSEA in TCGA cohorts and corresponding controls and helped with the bioinformatics data interpretation. H.T helped with the bioinformatics data interpretation. O.G analyzed the RNAseq data. G.G-L. and F.A. supervised ssGSEA in TCGA cohorts and helped with the interpretation of the bioinformatics data. C.M. helped with *in vitro* experiments and

qRT-PCR validations. C.T. helped with OT1 cytotoxicity assays in vitro and *MDK* mRNA levels in mouse melanoma cell lines. A.X.C and R.R performed the scRNA analysis and helped with the interpretation. L.M. helped with the flow cytometry analysis. N.I and J.M performed the proteomic analyses. T.G.C. helped with the animal sample processing and the mice colony maintenance. E.C. helped with the tissue culture experiments and Western Blot validations. The manuscript was written by M.S.S, D.C-W and D.O. and approved by all authors. M.S.S. and D.O. supervised the project.

Competing Interests statement

The authors declare no competing Interests

REFERENCES

1. Spranger, S. & Gajewski, T.F. Impact of oncogenic pathways on evasion of antitumour immune responses. *Nat Rev Cancer* **18**, 139-147 (2018).
2. Grivennikov, S.I., Greten, F.R. & Karin, M. Immunity, inflammation, and cancer. *Cell* **140**, 883-899 (2010).
3. Herrscher, H. & Robert, C. Immune checkpoint inhibitors in melanoma in the metastatic, neoadjuvant, and adjuvant setting. *Curr Opin Oncol* **32**, 106-113 (2020).
4. Havel, J.J., Chowell, D. & Chan, T.A. The evolving landscape of biomarkers for checkpoint inhibitor immunotherapy. *Nat Rev Cancer* **19**, 133-150 (2019).
5. Liu, D.*, et al.* Integrative molecular and clinical modeling of clinical outcomes to PD1 blockade in patients with metastatic melanoma. *Nat Med* **25**, 1916-1927 (2019).
6. Riaz, N.*, et al.* Tumor and Microenvironment Evolution during Immunotherapy with Nivolumab. *Cell* **171**, 934-949 e916 (2017).
7. Gide, T.N.*, et al.* Distinct Immune Cell Populations Define Response to Anti-PD-1 Monotherapy and Anti-PD-1/Anti-CTLA-4 Combined Therapy. *Cancer Cell* **35**, 238-255 e236 (2019).
8. Chen, P.L.*, et al.* Analysis of Immune Signatures in Longitudinal Tumor Samples Yields Insight into Biomarkers of Response and Mechanisms of Resistance to Immune Checkpoint Blockade. *Cancer Discov* **6**, 827-837 (2016).
9. Snyder, A.*, et al.* Genetic basis for clinical response to CTLA-4 blockade in melanoma. *N Engl J Med* **371**, 2189-2199 (2014).
10. Jerby-Arnon, L.*, et al.* A Cancer Cell Program Promotes T Cell Exclusion and Resistance to Checkpoint Blockade. *Cell* **175**, 984-997 e924 (2018).
11. Jiang, P.*, et al.* Signatures of T cell dysfunction and exclusion predict cancer immunotherapy response. *Nat Med* **24**, 1550-1558 (2018).

12. Neubert, N.J.*, et al.* T cell-induced CSF1 promotes melanoma resistance to PD1 blockade. *Sci Transl Med* **10**(2018).
13. Mantovani, A., Marchesi, F., Malesci, A., Laghi, L. & Allavena, P. Tumour-associated macrophages as treatment targets in oncology. *Nat Rev Clin Oncol* **14**, 399-416 (2017).
14. Thommen, D.S. & Schumacher, T.N. T Cell Dysfunction in Cancer. *Cancer Cell* **33**, 547-562 (2018).
15. Olmeda, D.*, et al.* Whole-body imaging of lymphovascular niches identifies pre-metastatic roles of midkine. *Nature* **546**, 676-680 (2017).
16. Sorrelle, N., Dominguez, A.T.A. & Brekken, R.A. From top to bottom: midkine and pleiotrophin as emerging players in immune regulation. *J Leukoc Biol* **102**, 277-286 (2017).
17. Jones, D.R. Measuring midkine: the utility of midkine as a biomarker in cancer and other diseases. *Br J Pharmacol* **171**, 2925-2939 (2014).
18. Sakamoto, K. & Kadomatsu, K. Midkine in the pathology of cancer, neural disease, and inflammation. *Pathol Int* **62**, 445-455 (2012).
19. Kadomatsu, K. The midkine family in cancer, inflammation and neural development. *Nagoya J Med Sci* **67**, 71-82 (2005).
20. Zhao, S.*, et al.* Midkine upregulates MICA/B expression in human gastric cancer cells and decreases natural killer cell cytotoxicity. *Cancer immunology, immunotherapy : CII* **61**, 1745-1753 (2012).
21. Guo, X.*, et al.* Midkine activation of CD8(+) T cells establishes a neuron-immune-cancer axis responsible for low-grade glioma growth. *Nat Commun* **11**, 2177 (2020).
22. Ohuchida, T.*, et al.* Midkine protects hepatocellular carcinoma cells against TRAIL-mediated apoptosis through down-regulation of caspase-3 activity. *Cancer* **100**, 2430-2436 (2004).
23. Ribas, A. & Wolchok, J.D. Cancer immunotherapy using checkpoint blockade. *Science* **359**, 1350-1355 (2018).
24. Herradon, G., Ramos-Alvarez, M.P. & Gramage, E. Connecting Metainflammation and Neuroinflammation Through the PTN-MK-RPTPbeta/zeta Axis: Relevance in Therapeutic Development. *Front Pharmacol* **10**, 377 (2019).
25. Weckbach, L.T., Preissner, K.T. & Deindl, E. The Role of Midkine in Arteriogenesis, Involving Mechanosensing, Endothelial Cell Proliferation, and Vasodilation. *Int J Mol Sci* **19**(2018).
26. Weckbach, L.T.*, et al.* The cytokine midkine supports neutrophil trafficking during acute inflammation by promoting adhesion via beta2 integrins (CD11/CD18). *Blood* **123**, 1887-1896 (2014).
27. Masuda, T.*, et al.* Growth Factor Midkine Promotes T-Cell Activation through Nuclear Factor of Activated T Cells Signaling and Th1 Cell Differentiation in Lupus Nephritis. *The American Journal of Pathology* (2017).
28. TCGA. Genomic Classification of Cutaneous Melanoma. *Cell* **161**, 1681-1696 (2015).
29. Liberzon, A.*, et al.* The Molecular Signatures Database (MSigDB) hallmark gene set collection. *Cell Syst* **1**, 417-425 (2015).
30. Shimoni, Y. Association between expression of random gene sets and survival is evident in multiple cancer types and may be explained by sub-classification. *PLoS Comput Biol* **14**, e1006026 (2018).
31. Yoshihara, K.*, et al.* Inferring tumour purity and stromal and immune cell admixture from expression data. *Nature Communications* **4**(2013).

32. Thorsson, V.*, et al.* The Immune Landscape of Cancer. *Immunity* **48**, 812-830 e814 (2018).
33. Weckbach, L.T., Muramatsu, T. & Walzog, B. Midkine in inflammation. *ScientificWorldJournal* **11**, 2491-2505 (2011).
34. Newman, A.M.*, et al.* Robust enumeration of cell subsets from tissue expression profiles. *Nature Methods* **12**, 453-457 (2015).
35. Poh, A.R. & Ernst, M. Targeting Macrophages in Cancer: From Bench to Bedside. *Front Oncol* **8**, 49 (2018).
36. Jewell, R.*, et al.* The clinicopathological and gene expression patterns associated with ulceration of primary melanoma. *Pigment Cell Melanoma Res* **28**, 94-104 (2015).
37. Perrotta, C.*, et al.* Nitric oxide generated by tumor-associated macrophages is responsible for cancer resistance to cisplatin and correlated with syntaxin 4 and acid sphingomyelinase inhibition. *Frontiers in Immunology* **9**(2018).
38. Liou, G.-Y.*, et al.* The Presence of Interleukin-13 at Pancreatic ADM/PanIN Lesions Alters Macrophage Populations and Mediates Pancreatic Tumorigenesis. *Cell Reports* **19**, 1322-1333 (2017).
39. Meeth, K., Wang, J.X., Micevic, G., Damsky, W. & Bosenberg, M.W. The YUMM lines: a series of congenic mouse melanoma cell lines with defined genetic alterations. *Pigment Cell Melanoma Res* **29**, 590-597 (2016).
40. Szklarczyk, D.*, et al.* STRING v10: protein-protein interaction networks, integrated over the tree of life. *Nucleic Acids Res* **43**, D447-452 (2015).
41. Kessenbrock, K., Plaks, V. & Werb, Z. Matrix metalloproteinases: regulators of the tumor microenvironment. *Cell* **141**, 52-67 (2010).
42. Dejonckheere, E., Vandenbroucke, R.E. & Libert, C. Matrix metalloproteinase8 has a central role in inflammatory disorders and cancer progression. *Cytokine Growth Factor Rev* **22**, 73-81 (2011).
43. Shabani, F., Farasat, A., Mahdavi, M. & Gheibi, N. Calprotectin (S100A8/S100A9): a key protein between inflammation and cancer. *Inflamm Res* **67**, 801-812 (2018).
44. Jones, S.A. & Jenkins, B.J. Recent insights into targeting the IL-6 cytokine family in inflammatory diseases and cancer. *Nat Rev Immunol* **18**, 773-789 (2018).
45. Lachmann, A.*, et al.* ChEA: transcription factor regulation inferred from integrating genome-wide ChIP-X experiments. *Bioinformatics* **26**, 2438-2444 (2010).
46. Sancho, D.*, et al.* Identification of a dendritic cell receptor that couples sensing of necrosis to immunity. *Nature* **458**, 899-903 (2009).
47. Enamorado, M.*, et al.* Enhanced anti-tumour immunity requires the interplay between resident and circulating memory CD8+ T cells. *Nature Communications* **8**(2017).
48. Ayers, M.*, et al.* IFN-gamma-related mRNA profile predicts clinical response to PD-1 blockade. *J Clin Invest* **127**, 2930-2940 (2017).
49. Curtsinger, J.M., Agarwal, P., Lins, D.C. & Mescher, M.F. Autocrine IFN-gamma promotes naive CD8 T cell differentiation and synergizes with IFN-alpha to stimulate strong function. *J Immunol* **189**, 659-668 (2012).
50. Orecchioni, M., Ghosheh, Y., Pramod, A.B. & Ley, K. Macrophage Polarization: Different Gene Signatures in M1(LPS+) vs. Classically and M2(LPS-) vs. Alternatively Activated Macrophages. *Front Immunol* **10**, 1084 (2019).
51. Li, H.*, et al.* Dysfunctional CD8 T Cells Form a Proliferative, Dynamically Regulated Compartment within Human Melanoma. *Cell* **176**, 775-789 e718 (2019).
52. Ascierto, M.L.*, et al.* Transcriptional Mechanisms of Resistance to Anti-PD-1 Therapy. *Clin Cancer Res* **23**, 3168-3180 (2017).

53. Hugo, W*., et al.* Genomic and Transcriptomic Features of Response to Anti-PD-1 Therapy in Metastatic Melanoma. *Cell* **165**, 35-44 (2016).
54. Van Allen, E.M*., et al.* Genomic correlates of response to CTLA-4 blockade in metastatic melanoma. *Science* **350**, 207-211 (2015).
55. Mariathasan, S*., et al.* TGFβ attenuates tumour response to PD-L1 blockade by contributing to exclusion of T cells. *Nature* **554**, 544-548 (2018).
56. Wei, S.C., Duffy, C.R. & Allison, J.P. Fundamental Mechanisms of Immune Checkpoint Blockade Therapy. *Cancer Discov* **8**, 1069-1086 (2018).
57. Cristescu, R*., et al.* Pan-tumor genomic biomarkers for PD-1 checkpoint blockade-based immunotherapy. *Science* **362**(2018).
58. Gajewski, T., Schreiber, H. & Fu, Y.-X. Innate and adaptive immune cells in the tumor microenvironment. *Nature immunology* **14**, 1014-1022 (2013).
59. Vasan, N., Baselga, J. & Hyman, D.M. A view on drug resistance in cancer. *Nature* **575**, 299-309 (2019).
60. Tirosh, I*., et al.* Dissecting the multicellular ecosystem of metastatic melanoma by single-cell RNA-seq. *Science* **352**, 189-196 (2016).

Online References

61. Liersch, R*., et al.* Analysis of a novel highly metastatic melanoma cell line identifies osteopontin as a new lymphangiogenic factor. *International journal of oncology* **41**, 1455-1463 (2012).
62. Berghaus, L.J*., et al.* Innate immune responses of primary murine macrophage-lineage cells and RAW 264.7 cells to ligands of Toll-like receptors 2, 3, and 4. *Comparative Immunology, Microbiology and Infectious Diseases* **33**, 443-454 (2010).
63. Olmeda, D*., et al.* Antimetastatic dsRNA mimics identified by live imaging of pathogenic neolymphangiogenesis. ***BiorXiv*** (2019).
64. Graña*, O., Rubio-Camarillo, M., Fdez-Riverola, F., Pisano, D.G. & Glez-Peña, D. Nextpresso: Next Generation Sequencing Expression Analysis Pipeline. *Current Bioinformatics* **13**, 583-591 (2018).
65. Wiśniewski, J.R., Zougman, A., Nagaraj, N. & Mann, M. Universal sample preparation method for proteome analysis. *Nature methods* **6**, 3-7 (2009).
66. Hänzelmann, S., Castelo, R. & Guinney, J. GSVA: gene set variation analysis for microarray and RNA-Seq data. *BMC Bioinformatics* **14**, 7 (2013).

FIGURE LEGENDS

Figure 1. MDK-driven gene expression changes in melanoma.

(**a**) Experimental set up for the –omic and functional characterization of MDK. (**b**) Distribution of TCGA metastatic melanoma patients as a function of the enrichment in MDK^{GOF} or MDK^{LOF} scores. The top and bottom 15^{th} percentile of patients in this

enrichment score (herein referred to as $MDK^{High\text{-}p}$ or $MDK^{Low\text{-}p}$ and labelled in red and blue, respectively) were selected for analyses of immune profiling and correlation to overall survival (Pearson correlation). (**c**) Kaplan-Meier curves of overall survival in $MDK^{High\text{-}p}$ (High), or $MDK^{Low\text{-}p}$ (Low), as selected in (**b**). *P*-values correspond to two-sided Log-Rank analyses. (**d**) Heatmap representing differentially expressed genes between $MDK^{High\text{-}p}$ and $MDK^{Low\text{-}p}$ patients grouped according to relevant biological processes. (**e**) Signalling cascades from MSigDB related to immunomodulation found significantly enriched in the $MDK^{High\text{-}p}$ vs $MDK^{Low\text{-}p}$ metastatic TCGA melanomas (FDR q-value <0.25, GSEA). See data in Supplementary Table 6. (**f**) Enrichments for IFN-γ score (left) and TGF-β score[32] (right), estimated by CIBERSORT and Ref[32] from in $MDK^{High\text{-}p}$ vs $MDK^{Low\text{-}p}$ samples (Low, *n* = 30; High = 42; multiple comparison using Two-tailed t-test and Holm-Sidak correction). (**g**) *IL13* (left) and *IL10* (Right) mRNA levels in $MDK^{High\text{-}p}$ vs $MDK^{Low\text{-}p}$ patients (Low, *n* = 30; High = 42; unpaired two-tailed t-test). (**h**) Enrichments for the indicated immune cell populations as calculated by Ref[32] from in $MDK^{High\text{-}p}$ vs $MDK^{Low\text{-}p}$ samples (Low, *n* = 30; High = 42; unpaired two-tailed t-test). (**i**) Enrichment of macrophage-specific transcriptional signature[12] in $MDK^{High\text{-}p}$ or $MDK^{Low\text{-}p}$ TCGA-melanomas. NES, normalized enrichment score. In all boxplots in this figure, the median is indicated by the horizontal line and the first and third quartiles by the box edges. The lower and upper whiskers extend from the hinges to the smallest and largest values, respectively, with individual values included.

Figure 2. MDK favours intratumoural recruitment of myeloid cells with suppressive features.

(**a**) Immunofluorescence microscopy for MDK (green) and Arg1 (red) in xenografts of WM164 transduced with lentiviruses coding for MDK or their control vector. (**b**) Representative histograms showing intratumoural Arg1-expressing cells in B16-MDK vs Control tumours, with the corresponding quantifications (**c**), as assessed by flow

cytometry. Ctrl, *n* = 4; MDK = 5 tumours. Unpaired two-tailed Mann Whitney Test. (**d**) Quantification of intratumoural myeloid cells ($CD45^+CD11b^+$) in loss of function (LOF) analyses of implants of B16R2L transduced with shControl (shC, red) or shMDK (blue). (**e**) $CD45^+CD11b^+$ in gain of function (GOF) analyses of B16F1 transduced with empty plasmid (Control, blue) or with MDK-expressing lentiviral vector (MDK, red). Ctrl, *n*= 4; MDK = 5 tumours. Unpaired two-tailed t-test. (**f-h**) Additional immune cell populations in MDK-GOF as in (**e**): $CD11b^+Ly6C^+Ly6G^-$ (**f**), $Arg1^+$ monocytes (**g**) and $Arg1^+$ macrophages ($F4/80^+Arg1^+$) (**h**). *n* = 5 tumours. Unpaired two-tailed t-test. **(i)** Pie-charts representing the percentage of indicated cell populations from total intratumoural immune cells ($CD45^+$) infiltrating early lesions (tumour size<200mm^3) from B16F1-MDK transplants compared to control, as measured by flow cytometry. Ctrl, *n*= 8; MDK, 7 tumours. Indicated with an asterisk are significantly altered populations unpaired two-tailed t-test). DC1 ($CD11b^+CD11c^+MHCII^+CD24^+CD103^+$), DC2 ($CD11b^+CD11c^+MHCII^+CD24^+CD103^-F4/80^-$, *P* = 0.0441), monocytes ($CD11b^+Ly6C^+Ly6G^-$, *P* = 0.0139), TAMs ($CD11b^+Ly6G^-F4/80^+$, *P* = 0.0016), neutrophils ($CD11b^+Ly6C^+Ly6G^+$), $CD8^+$ T cells ($CD3^+CD8^+$); $CD4^+$ T cells ($CD3^+CD4^+FoxP3^-$), Tregs ($CD3^+CD4^+CD25^+FoxP3^+$, *P* = 0.0171), NK ($CD3^-NK1.1^+$), NKT ($CD3^+NK1.1^+$). (**j**) qRT-PCR analysis of *Arg1* expression in bone marrow-derived macrophages (BMDM) differentiated with GM-CSF+IL-6 for 5 days (left) and murine macrophage cell line RAW264.7 (right) treated with the secretome of WM164 (Ctrl) or WM164-MDK for 48 hrs. Data are normalized to basal levels. *n*= 3 independent experiments in triplicate. Unpaired Two-Tailed T-test. (**k**) Immunoblots showing Arg1 expression in BMDM at indicated time points after incubation with recombinant MDK (10 ng/ml). **(l**) qRT-PCR analysis of *Arg1* expression in BMDM treated with indicated doses of recombinant MDK for 48 hrs. *n*= 3 independent experiments in triplicate; one-way ANOVA with Dunnet Correction. Data are normalized to basal levels. (**m**) *Arg1*

mRNA expression in BMDM differentiated with MCSF for 5 days and treated for 24 h with recombinant MDK (10 ng/ml), vehicle control (left), or with the secretome of WM164 (Ctrl) or WM164-MDK. *n*= 3 independent experiments in triplicate. Unpaired two-tailed t-test. (**n**) qRT-PCR analysis of *Arg1* expression in BMDM differentiated with MCSF for 5 days and treated with the secretome of human MDK^{High} cell line SK-Mel-147 (shC) or depleted for MDK (shMDK) for 24h. Data are normalized to basal levels. *n*= 3 independent experiments in triplicate. Unpaired two-tailed t-test. (**o**) Heatmap representing differentially expressed genes of human macrophages differentiated with MCSF for 6 days and treated with the secretome of human cell line SK-Mel-147 (shCtrl) or depleted for MDK (shMDK) for 24h. Data are normalized to basal levels. *n*= 3 independent experiments. Multiple comparison using two-tailed t-test and Holm-Sidak correction. Unless otherwise indicated, data in graphs correspond to mean ± s.d. Data shown correspond to a representative example out of 3 independent experiments. Box plots show median with 25^{th}/75^{th} percentiles and whiskers from minimum to maximum, and individual values are plotted.

Figure 3. Signalling networks underlying immunomodulatory roles of MDK

(**a**) Enrichment plot for "Hallmark TNFα signalling via NF-κB" identified by GSEA in RNAseq expression data from WM164 Control vs WM164-MDK (GOF settings). (**b**) Volcano plot showing secreted proteins found by LC/MS-MS to be upregulated or downregulated (red and blue, respectively) in WM164-MDK vs WM164-Control. The hyperbolic black curve separates differentially regulated proteins as defined by two-sample Student's t-test, FDR < 0.01; SO < 0.8. *n*= number of proteins. (**c**) STRING network analysis of immune-related proteins in MDK-driven secretome. Indicated are fold-induction values in WM164-MDK vs Control cells for each protein. (**d**) Top-left, Levels of secreted MDK (by ELISA) in the indicated cell populations: WM164 (melanoma), A549 (LUSC), and U87 (glioma) for GOF settings, and SK-Mel-147

(melanoma) for LOF. Data in graphs correspond to mean ± s.d. Top-right, MDK in murine lines YUMM2.1 and B16F1 transduced with MDK, as well as in B16R2L depleted for MDK (the latter defined by RT-PCR). Data are mean ± s.d. Bottom panels: RelA (p65) activity in the indicated cell lines, as assessed by a dual-reporter Firefly/Renilla luciferase RelA-activity assay. *n* = 6 independent experiments (unpaired two-tailed t-test). (**e-f**) qRT-PCR analysis of NF-κB related genes in WM164-MDK melanoma cells (**e**) and the murine YUMM2.1-MDK (**f**), represented with respect to the parental controls (dashed line). (**g**) qRT-PCR analysis of *S100a8* mRNA in MDK expressing murine melanoma cells vs control (YM2.1=YUMM2.1; YM1.1=YUMM1.1; YMR1.7=YUMMER1.7). (**h**) qRT-PCR analysis of NF-κB related genes in cell line B16R2L depleted of MDK, compared to shCtrl parental counterpart (dashed line). Data shown in panels (**e-h**) correspond to significant deregulated genes ($P < 0.05$) from triplicates analysed by multiple comparison using two-tailed t-test with Holm-Sidak correction. (**i**) Relative mRNA levels of *IL6* or *TNF* in parental WM164 cells (blue) or WM164-MDK in non-treated conditions (red) or incubated in with the IKK-2 inhibitor (green, 1 μM TPCA-1, 24 hours). (**j**) *Arg1* mRNA levels in BMDM treated with conditioned medium from (**i**). (**k**) Relative mRNA levels of *Arg1*, *S100a8,* and *Nos2* in BMDM treated with conditioned medium from WM164 cells (blue), WM164-MDK (red) or WM164-MDK in which RELA has been previously inactivated by means of siRNA (green). Data in (**i**), (**j**) and (**k**) were obtained by qRT-PCR performed in independent triplicates, one-way ANOVA with Tukey post-test. Graphs in **(e-k**) plot data as mean ± s.d. and correspond to a representative example out of 3 independent experiments in triplicate. Box plots show median with $25^{th}/75^{th}$ percentiles and whiskers from minimum to maximum, and individual values are plotted.

Figure 4. MDK induces resistance to immune checkpoint blockade in mice.

Quantification of anti-OVA IgG1 levels in blood after OVA vaccination, as measured by ELISA. Ctrl, *n* = 4; MDK = 3. Multiple comparison using two-tailed t-test with Holm-Sidak correction. (**b**) Growth curves of Control and MDK B16-OVA tumours in OVA-immunized (I) or non-immunized (NI) mice as explained in Methods. *n* = 6 mice per condition. Shown are mean ± s.e.m.; two-way ANOVA with Bonferroni post-test. Indicated is the *P*-value of MDK vs Control B16-OVA tumours in OVA-immunized mice. (**c**) Percentage of myeloid cells ($CD11b^+$, left) or $CD8^+$ T cells (right) within immune cells ($CD45^+$) in tumours from (**b**), as assessed by flow cytometry. *n = 3* biological replicates. Multiple comparison using Two-tailed t-test with Holm-Sidak correction. (**d**) Growth curves of parental B16-OVA tumours (left) or their MDK-overexpressing isogenic pair (right) implanted in immunocompetent mice and treated with IgG2a isotype control (10 mg/Kg) or αPD1 antibody (clone RMP1-14, 10 mg/Kg) on indicated days (arrows). Treatments performed in the presence of MDK inhibitor (iMDK, 9mg/kg) are labelled in purple. Ctrl, *n* = 5; MDK *n* = 4 mice; mean ± s.e.m; two-way ANOVA with Bonferroni post-test. Indicated is the significant difference (*P*-value) between MDK B16-OVA tumours αPD1 treated vs αPD1+MDKi. (**e**) Kaplan-Meier curves of overall survival of mice implanted with B16R2L (shC) or B16R2L-shMDK tumours and treated with IgG2a isotype control (5 mg/Kg) or αPD1 antibody (clone RMP1-14, 5 mg/Kg). Shown is the *P* -value of the shMDK + αPD1 combination with respect to the shC + IgG2a control; two-sided Log-Rank test; Samples sizes are shC+gG2a = 6, shC+PD1 = 7, shMDK + IgG2a = 7, shMDK + IPD1 = 9 mice. (**f**) MSigDB Hallmark Gene set collection identified by GSEA to be differentially upregulated in tumours B16R2L shMDK vs shCtrl, without treatment (grey) and upon αPD1 treatment (green, FDR q-value <0.25). (**g**) Heatmap showing the differential expression of genes from IFN-γ-

related pathways (from Hallmarks collection), “M1”-like antitumoural macrophages (MΦ)[50] and T cell infiltration[10] in the indicated experimental groups. Highlighted are representative genes with known roles in ICB-response in patients. (**h**) Enrichment plot of IFN-γ-related genes and in Macrophages M1” gene signature in B16R2L tumors with respect to the shMDK-αPD1 combination. (**i**) Example of histological stainings showing levels of $CD8^+$ T cells (pink) in tumours from (**e**), with corresponding quantifications in (**j**). n=4 technical replicates in 3 biological replicates. Multiple comparison using two-tailed t-test with Holm-Sidak correction. Box plots show median with $25^{th}/75^{th}$ percentiles and whiskers from minimum to maximum, plotting individual values.

Figure 5. MDK–educated macrophages drive T cell dysfunction.

(**a**) Percentage of intratumoural monocytes ($CD11b^+Ly6C^+Ly6G^-$) in B16F1-OVA-MDK implants (red) or the parental control (blue) after pharmacological depletion of monocyte/macrophages with αCSF1R antibody (clone AFS98, 20 mg/Kg). IgG2a isotype was used as control (20 mg/Kg). *n* = 8 mice per condition. Two-way ANOVA with Tukey Post-test. Box-plot represents minimum, maximum, median, $25^{th}/75^{th}$ percentiles, plotting all points. (**b**) Growth curves of control (left) or B16F1-OVA-MDK (right) treated with αCSF1R in the absence or presence of αPD1 (clone RMP1-14, 10 mg/Kg) at the indicated days (arrows). *n* = 8 mice per condition. Data correspond to mean ± s.e.m. Shown are significant P-values obtained by two-way ANOVA with Tukey Post-test. (**c**) OT-1 T cell killing of B16-OVA-Control (Blue) or B16-OVA-MDK (red) in the presence of BMDM. *n* =3 independent replicates. Data in graphs correspond to mean ± s.d, including significant *P*-values; two-way ANOVA with Bonferroni post-test. (**d**) OT-1 killing of B16-OVA-MDK in the absence or presence of BMDM (red and

yellow, respectively), and upon RelA inactivation by siRNA (green). Data in graphs correspond to mean ± s.d. n=3 independent replicates, one-way ANOVA with Tukey post-test. (**e**) OT-1 killing of B16-OVA-MDK (red), in the presence of BMDM (yellow), and upon Arg1 pharmacological inhibition (green, ABH; 500nM). Mean ± s.d; *n* =3 independent replicates, One-way ANOVA with Tukey post-test. (**f**) Relative mRNA levels of *Plaur*, *Havcr2* and *Eomes* in OT1 cells after 24 h co-culture with BMDM pre-conditioned with the secretome of MDK-YUMM2.1 cell (red) or control counterparts (blue). *n* =3 independent experiments in triplicate; mean ± s.d.; unpaired two-tailed T-test. (**g**) Enrichment score for the "Dysfunctional $CD8^+$/Naïve" signature[51] and (**h**) the "T cell dysfunction Signature" (TIDE)[11] in TCGA melanoma patients with $MDK^{HIgh\text{-}p}$ vs $MDK^{Low\text{-}p}$ (NES=normalized enrichment score, FDR q-Value). (**i**) Prediction of clinical response to immune checkpoint blockade in $MDK^{High\text{-}p}$ vs $MDK^{Low\text{-}P}$ metastatic melanoma patients using the TIDE gene expression platform[11], with the corresponding *P* - value.

Figure 6. MDK correlates with immunotherapy resistance in melanoma patients.

(**a**) Enrichment score of the indicated signatures for good prognosis in ICB-treated patients estimated from the differentially expressed genes of implants of B16R2L shMDK vs shCtrl, in mice treated with αPD1 (see text). (**b**) Heatmap representing deregulated genes in implants of B16R2L shMDK vs shC tumour cells, in mice treated with IgG2a control or αPD1 as indicated. Shown are the top 100 genes in the [$shMDK^{up}$-ICB^{up}] category and all the [$shMDK^{down}$-ICB^{down}]. (**c**) Left, representative examples of genes in (**b**), previously described as associated with ICB response in (1)-Ref[6]; (2)-Ref[7] (αPD1); (3)-Ref[48]; (4)-Ref[8]; (5)- Ref[7]; or related to (6)-IFN-γ- (from Hallmarks collection; M5913); (7)-"M1" macrophages[50] or (8) T cell infiltration[10]. "This

study" highlights genes not reported in these datasets (1)-(8). (**d**) Kaplan-Meier analysis of overall survival in patients treated with αPD1 (Cohort 1, Ref[7]) or αCTLA4 (Cohort 5, Ref[54]). Patients within the top 25th percentile (red) and the bottom 25th percentile (blue) of shMDK-ICB-Score were compared. Two-sided Log-Rank test. See Extended Figure 10 for additional cohorts. (**e**) Analysis of the shMDK-ICB score between responders (R) and not responders (NR) in patients early during treatment (EDT) in Cohort 1 (Ref[7]) and in patients on treatment in Cohort 2 (Ref[6]). Number of patients in Cohort 1 (R = 9, NR = 7); Cohort 2 (R = 10, NR = 21). Box plots show median with 25th/75th percentiles and whiskers from minimum to maximum, plotting individual values.Two-tailed t-test. (**f**) Summary of the main conclusions from this study. In brief, MDK was found to rewire the transcriptome and proteome of melanoma cells to promote an immune suppressive background driven in part by NF-κB. This secretome was enriched in factors such as S100A8/9, CCL2/3, TGFB1, IL6 and CSF1, among others, able to attract and reprogram macrophages towards suppressive phenotypes (exemplified by ARG1). This microenvironment ultimately leads to CD8 T cell dysfunction (with characteristic markers such as PLAUR, HACVR2, or EOMES, also in a TGFB1 context). In the absence of MDK, this suppressive background was found to shift to a proinflammatory IFN-associated response, now with macrophage polarization towards antitumoural phenotypes, enhanced CD8 T cell recruitment, and increased sensitivity to ICB treatment. The relevance of the shMDK-ICB combination was demonstrated in independent patient cohorts.

Extended Figure 1. Bioinformatic analyses of MDK-associated gene expression profile in TCGA patients.

(**a**) Kaplan-Meier analysis showing the survival probability of the patients expressing high (n = 54) and low (n = 55) *MDK* mRNA levels (top and bottom 15th percentile in the metastatic melanoma TCGA dataset, respectively). Two-sided Log-Rank (Mantel-Cox) test. (**b**) Heatmap showing relative mRNA levels (defined by RNAseq) in the indicated cell populations corresponding to gain or loss of function of MDK (GOF and LOF) . See Supplementary Table 1 and 2 for complete gene lists. (**c-f**) Controls to rule out random bias in the MDK-associated gene profile. 10,000 gene sets with the same size as the original MDK GOF and LOF profiles, were tested by ssGSEA for enrichment in TCGA-metastatic melanoma as in Fig. 1b. Pearson correlation coefficient, -0.56 < *r* <0.52, mean: -0.002 (**c**); *R* squared correlation index (**b**); *P*-value (**d**) and FDR (**e**). (**g**) Kaplan-Meier curves of overall survival in patients within the 15th percentile with an MDK$^{High\text{-}p}$ (red) or a MDK$^{Low\text{-}p}$ (blue) in TCGA patient cohorts of Lung Squamous Cell Carcinoma (LUSC, MDK$^{High\text{-}p}$ *n* = 33; MDK$^{Low\text{-}p}$ = 30), Glioblastoma (GBM, MDK$^{High\text{-}p}$ *n* = 10; MDK$^{Low\text{-}p}$ = 13) or Kidney Renal Clear Cell Carcinoma (KIRC, MDK$^{High\text{-}p}$ *n* = 53; MDK$^{Low\text{-}p}$ = 48). Log-rank (Mantel-Cox) test.

Extended Figure 2. Immune profiles associated to MDK in TCGA-patients.

(**a-b**) Box-plots depicting proliferation score (**a**) , ImmuneScore (**b**, left) and Leukocyte Score (**b**, right) in MDK$^{High\text{-}p}$ vs MDK$^{Low\text{-}p}$ patients. Low MDK, n= 30; High MDK = 42 (defined as in Fig. 1b). Unpaired Two-Tailed T-test. (**c**) Scores of the indicated immune cell populations in MDK$^{High\text{-}p}$ vs MDK$^{Low\text{-}p}$ samples. Low MDK, n= 30; High MDK = 42. Multiple comparison using two-tailed t-test with Holm-Sidak correction. (**d**) Violin plots showing the enrichment of the MDK$^{High\text{-}p}$ score within the indicated cell populations, generated from scRNA-seq of melanoma samples[60] (*n* =2887 cells) and defined by ssGSEA. Statistical differences among cell populations compared as indicated were

estimated by two-tail Mann-Whitney test. (**e**) UMAP showing the identification of the different populations of cells (left panel), and their corresponding Enrichment Score Rank (Right panel), for data from (**d**). (**f**) TGF-β, Tregs and macrophage score, for patients within the 15th percentile of MDK$^{High\text{-}p}$ (red) or MDK$^{Low\text{-}p}$ (blue) of Lung Squamous Cell Carcinoma (LUSC, left), Glioblastoma (GBM, middle) or Kidney Renal Clear Cell Carcinoma (KIRC, right) from TCGA. Information was extracted from previously reported immunogenomic data[32]. Unpaired two-Tailed t-test. (**g**) Representative histological staining showing levels of CD163 (level 1-3) and MDK in these patients. CD163 L1 (*n* = 32), CD163 L2 (*n* = 85) and L3 groups (*n* = 68). (**h**) Summary of multivariate analysis of MDK expression and the indicated tumour-associated features in patients from an independent cohort of stage III melanoma patients. In all boxplots in this figure, the median is indicated by the horizontal line and the first and third quartiles by the box edges. The lower and upper whiskers extend from the hinges to the smallest and largest values, respectively, with individual values included.

Extended Figure 3. MDK favours the intratumoural recruitment of ARG1^{+} cells.

(**a**) Immunofluorescence microscopy for MDK (green), TAM marker YM1 (red), and iNOS (grey) in WM164-MDK vs Control xenografts. (**b**) Immunofluorescence microscopy for MDK (green) and Arg1 (red) in B16F10-MDK vs Control tumours. (**c**) *MDK* mRNA levels assessed by qRT-PCR in indicated mouse melanoma cell lines. YM2.1 (YUMM2.1), YM1.1 (YUMM 1.1) and YUMMER 1.7 (YMR1.7). Data in graphs correspond to mean ± s.d. *n* = 3 biological replicates. (**d**) MDK secretion in human melanoma cell lines SK-Mel-147 (shCtrl vs shMDK), and WM164 (Control vs MDK); mouse melanoma cell lines YM2.1 (YUMM2.1), YM1.1 (YUMM1.1) and YUMMER1.7 (YMR1.7) upon MDK overexpression (red); human LUSC cell lines (green); and human

GBM (Yellow), as assessed by ELISA. Data in graphs correspond to mean ± s.d. *n* = 3 biological replicates. (**e-g**) Gating strategy for flow cytometry assays in this study: $Arg1^+$ myeloid cells (**e**); myeloid cells, including dendritic cell populations (**f**), or lymphocytes (**g**). Neu = neutrophils; Mo = monocytes; TAMs = tumour associated macrophages; DC1 = dendritic cells type 1; DC2 = dendritic cells type 2; $CD4^+$ T cells = T helper cells; $CD8^+$ T =T cytotoxic cells; Tregs = regulatory T cells.

Extended Figure 4. Immunophenotyping of MDK-expressing tumours.

(**a**) Representative histograms of intratumoural myeloid cells ($CD11b^+$) in B16-R2L implants upon MDK depletion (shMDK, LOF), and in B16F1 tumours upon MDK expression (GOF). (**b**) Quantification of total $Ly6G^+Ly6C^+$ granulocytic/neutrophil cells (left) and $Arg1^+$ neutrophils in B16F10 tumours upon MDK expression, as measured by flow cytometry. *n* = 5 mice per condition. Unpaired two-tailed t-test. (**c**) Quantification of the indicated cell populations within immune cells infiltrating B16F1 tumours upon MDK-expression, as measured by flow cytometry. Control, *n* = 8; MDK = 7 tumours. Unpaired Two-Tailed T-test. (**d**) *Arg1* mRNA expression in tumours from (**c**). Unpaired two-tailed t-test . (**e**) Pie-charts indicating the percentage of indicated cell populations from total intratumoural immune cells ($CD45^+$) in B16R2L tumours upon MDK depletion, as measured by flow cytometry. Control, *n* = 4; MDK = 4 tumours. Indicated with an asterisk are significantly altered populations $P<0.05$. Two-tailed T-test. DC1 ($CD11b^+CD11c^+MHCII^+CD24^+CD103^+$), DC2 ($CD11b^+CD11c^+MHCII^+CD24^+CD103^-F4/80^-$), monocytes ($CD11b^+Ly6C^+Ly6G^-$, P = 0.0217), TAMs ($CD11b^+Ly6G^-F4/80^+$, P = 0.0405), neutrophils ($CD11b^+Ly6C^+Ly6G^+$), $CD8^+$ T cells ($CD3^+CD8^+$); $CD4^+$ T cells ($CD3^+CD4^+FoxP3^-$), Tregs ($CD3^+CD4^+CD25^+FoxP3^+$), NK ($CD3^-NK1.1^+$), NKT ($CD3^+NK1.1^+$). (**f**) Quantification of indicated cell populations from (**e**), as measured by flow cytometry. *n* = 4 tumours,

unpaired two-tailed t-test . Data shown correspond to a representative example out of 3 independent experiments. All box-plots in the figure represent minimum, maximum, median $25^{th}/75^{th}$ 5th/75th percentiles, and contain individual points.

Extended Figure 5. Transcriptomic and proteomic analyses of downstream effectors of MDK.

(**a**) MSigDB Hallmark Gene set collection identified by GSEA to be differentially expressed in the RNAseq of WM164-MDK vs WM164-Control melanoma cells. Data are plotted with respect to Normalized Enriched Scores (NES), with those representing downregulation and upregulation in blue and red, respectively. FDR q-value < 0.25. (**b**) Heatmap representing differentially expressed immunomodulatory proteins secreted by WM164 MDK melanoma cells with respect to their isogenic control. Relative expression values are represented as in the scale drawn in the bottom part of the figure.

Extended Figure 6. MDK and NF-κB associated signaling

(**a**) Predicted Transcription Factors (TF) (Enrichr-ChEA2016) regulating the MDK-induced secretome. Data represent Log10 of the *P* - value of the top 10 TF identified. (**b**) Western blot analysis of total and phosphorylated p65 (p-p65) at Ser536, in starved WM164 melanoma cells upon treatment with recombinant MDK (10 ng/ml), or with TNF (10 ng/ml) as a control. Representative example of three independent replicates. (**c**) Relative *Arg1* and *Il6* mRNA levels in BMDM cultured with the secretome from WM164 cells (blue) or the WM164-MDK isogenic pair control (red), previously treated with vehicle or αCalprotectin (αS100A8/A9) antibody, as assessed by qRT-PCR. *n* = 3 independent experiments; two-way ANOVA with Tukey post-test. (**d**) Relative *RelA*

mRNA levels in WM164 (left panel) and B16-OVA (right panel) 36h after RelA targeting by means of siRNA. Two-way ANOVA with Tukey Post-test. Data represent average ± s.d.; *n* = 3. (**e**) Cell viability in B16-OVA melanoma cells 48h after RelA targeting by means of siRNA, as assessed by Flow Cytometry analysis of Annexin V and Dapi. Left= representative dot plots, Righ= quantification. Two-way ANOVA with Tukey Post-test. Data represents average ± s.d; *n* = 3 independent experiments. Box plots show median with 25^{th}/75^{th} percentiles and whiskers from minimum to maximum, plotting all individual values.

Extended Figure 7. MDK promotes αPD1/PDL1 therapy resistance in mice.

(**a**) Experiment setup to assess the impact of MDK on an OVA-based vaccination assay. Shown are the different steps to vaccinate mice with the OVA protein, followed by subcutaneous implantation of parental B16-OVA melanoma cells (blue) or their isogenic MDK-expressing counterparts (red). 5 days after cell implantation, mice were rechallenged with LPS in the absence of OVA (non immunized, NI) or in the presence of OVA (immunized, I). (**b**) Immunohistochemical staining for MDK (red, top panels) and Arg1 (pink, bottom panels) in B16-OVA Control vs B16-OVA-MDK xenografts in non-immunized or immunized settings as indicated. (**c**) Growth curves of B16-OVA-MDK tumours (vs isogenic pair control) treated with IgG2a isotype control (10 mg/Kg) or αPD1 (clone RMP1-14, 10 mg/Kg) at the indicated days (arrows). Data correspond to average ± s.e.m.; *n* = 5 mice per condition. Statistical difference *(P* - value, two-way ANOVA with Tukey Post-test) between MDK vs Control B16-OVA tumours upon αPD1 treatment is indicated. (**d**) Quantification of intratumoural macrophages ($CD11b^{+}Ly6G^{-}F4/80^{+}$), $CD8^{+}PD1^{+}$ T cells, Treg ($CD4^{+}FoxP3^{+}CD25^{+}$), and CD8/Treg ratio by flow cytometry at the endpoint of (**c**). *n* = 4 tumours per condition. (**e**) Growth curves of B16-

OVA-MDK tumours (vs isogenic pair control) treated with IgG2b isotype control (10 mg/Kg) or αPDL1 blocking monoclonal antibody (clone 10F.9G2, 10 mg/Kg) at the indicated days (arrows). Data represent mean ± s.e.m. *n* = 5 mice per condition, with significant differences between MDK vs Control B16-OVA tumours upon αPDL1 treatment as indicated. (**f**) Circulating $CD8^+PD1^+$ T cells, Treg, and estimation of CD8/Treg ratio (mean ± s.e.m) defined by flow cytometry at the endpoint of the experiment in (**e**). n = 5 tumours per group. Data in **c-f** were analysed by two-way ANOVA with Bonferroni post-test. Box plots show median with 25th/75th percentiles and whiskers from minimum to maximum, plotting all individual values.

Extended Figure 8. MDK depletion enhances ICB efficacy.

(**a**) Growth curves of B16R2L tumours generated by control (shCtrl) or MDK-depleted (shMDK), in mice treated with IgG2a isotype control (10 mg/Kg) or αPD1 (clone RMP1-14, 10 mg/Kg) at the indicated days (arrows). *n* = 6 mice per condition; average ± s.e.m. (**b**) Spider-plots depicting individual tumour growth from (**a**). (**c,d**) MSigDB Hallmark Gene set collection identified by GSEA to be differentially expressed in the RNAseq of B16R2L shMDK vs shCtrl tumors in mice without treatment (**c**) and upon αPD1 treatment (**d**). Data are plotted with respect to Normalized Enriched Scores (NES), with those representing downregulation and upregulation in red and blue, respectively. FDR *q* - value <0.25. (**e**) Enrichment score for the GO "Acute Immune Response" (**GO**:0002526), in the transcriptome of MDK-depleted B16R2L tumours treated with IgG2a isotype control (left) or αPD1 (right).

Extended Figure 9. Impact of monocyte/macrophage depletion in MDK-associated responses and correlations with ICB signatures.

(**a**) Experimental procedure for the depletion of inflammatory monocytes using αCSF1R blocking monoclonal antibody (clone AFS98, 20 mg/Kg), and treatment with αPD1 (clone RMP1-14, 10 mg/Kg) at the indicated days. (**b**) Gene expression signatures correlating with resistance to ICB in the indicated studies. Highlighted in red are genes differentially upregulated between $MDK^{High\text{-}p}$ and $MDK^{Low\text{-}p}$ metastatic melanoma TCGA patients. Indicated are enrichment (FDR q-values) for each gene signature in $MDK^{High\text{-}p}$. (**c**) Correlation between the TIDE dysfunctional score[11] and the MDK^{GOF} score (from differentially expressed genes upon MDK depletion in melanoma cells, Supplementary Table 2) in patients with metastatic melanoma (SKCM*; n* = 316), glioblastoma (GBM; *n* = 151), lung squamous cell carcinoma (LUSC; n = 484), and kidney renal clear cell carcinoma (KIRC; *n* = 153) from the TCGA database.

Extended Figure 10. MDK correlates with ICB resistance in melanoma patient cohorts

(**a**) Enrichment score for the "good prognosis to ICB" Signature 5 (Ref[7], responders to αPD1+αCTLA4) in the differentially expressed genes of the shMDK-ICB combination, identified in B16R2L LOF experiments as in Fig. 6a. (**b**) Enrichment score for the indicated "good prognosis to ICB" signatures listed in the text (see **Supplementary Table 7**) in shMDK-depleted B16R2L tumours (data with respect to shC). (**c**) Kaplan-Meier analysis of overall survival in the indicated patient cohorts comparing patients within the top 25th percentile (red) and the bottom 25th percentile (blue) of MDK-ICB-Score. Two-sided Log-Rank test. (**d**) Progression-free survival in the indicated patient cohorts generated as in (**c**). Two-sided Log-rank (Mantel-Cox) test. Cohort 1 (Ref[7]), Cohort 2 (Ref[6]), Cohort 3 (Ref[5]), Cohort 4 (Ref[53]), Cohort 5 (Ref[54]), and Cohort 6 (Ref[9]).

Cerezo-Wallis et al. Figure 1

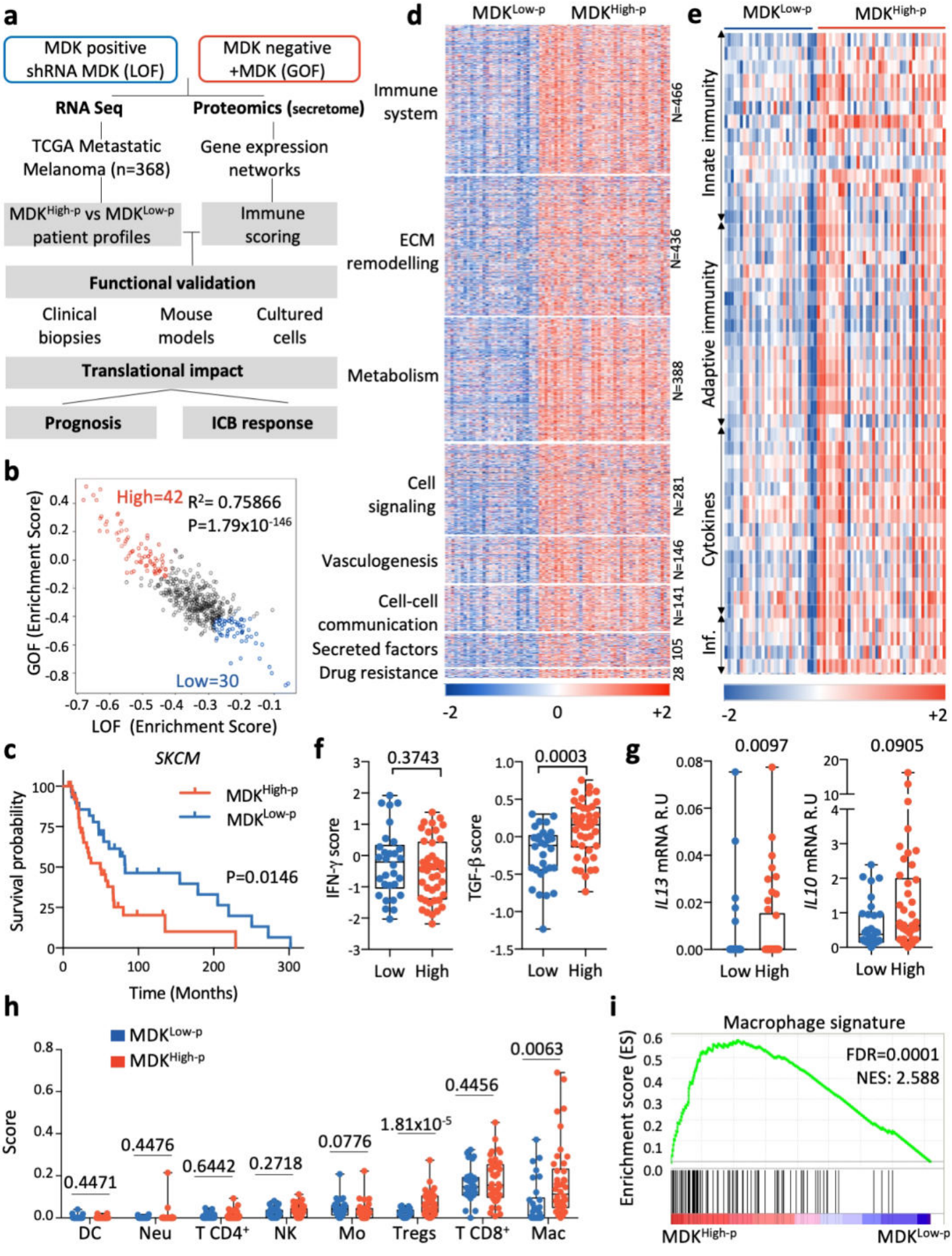

Cerezo-Wallis et al. Figure 2

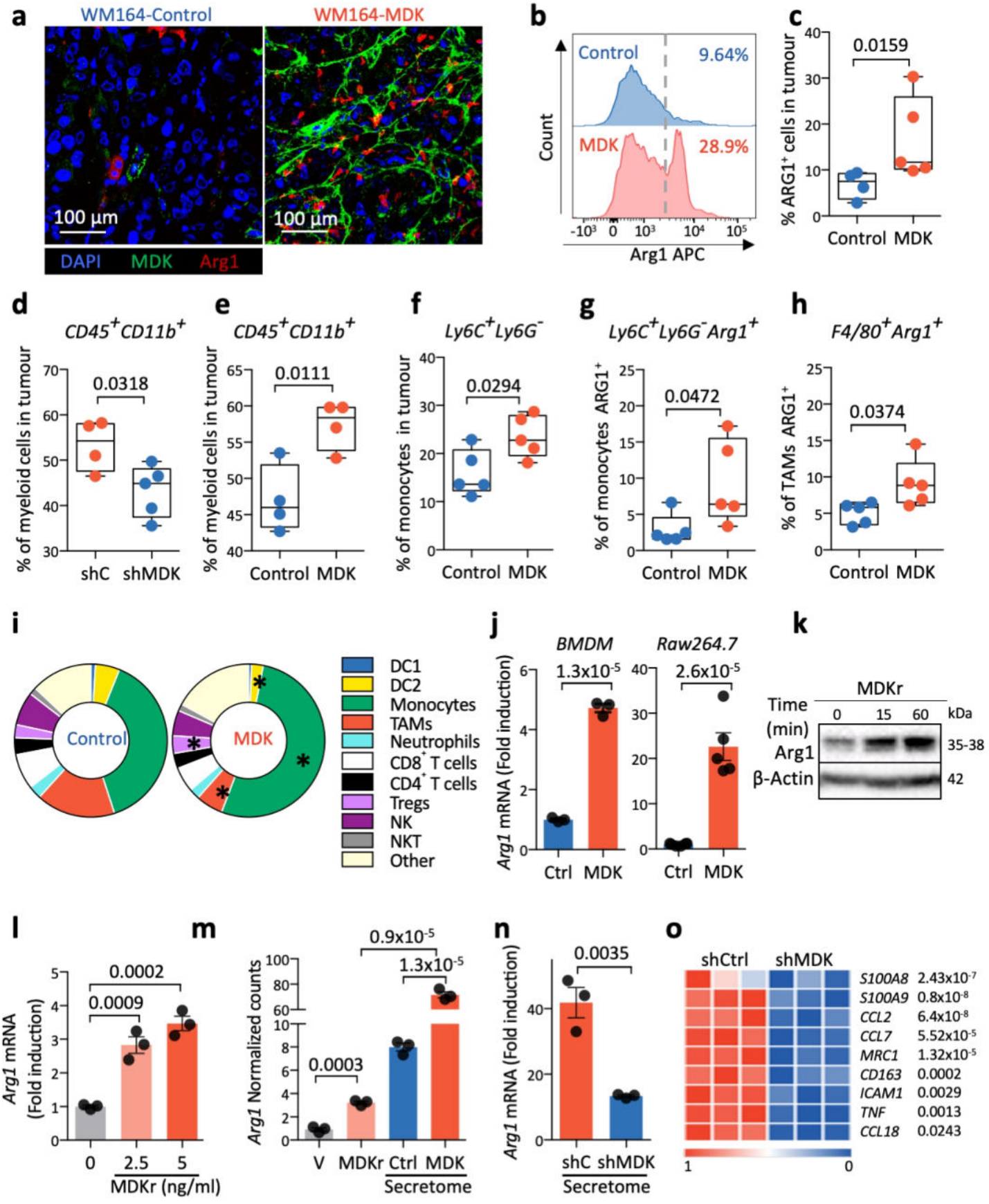

Cerezo-Wallis et al. Figure 3

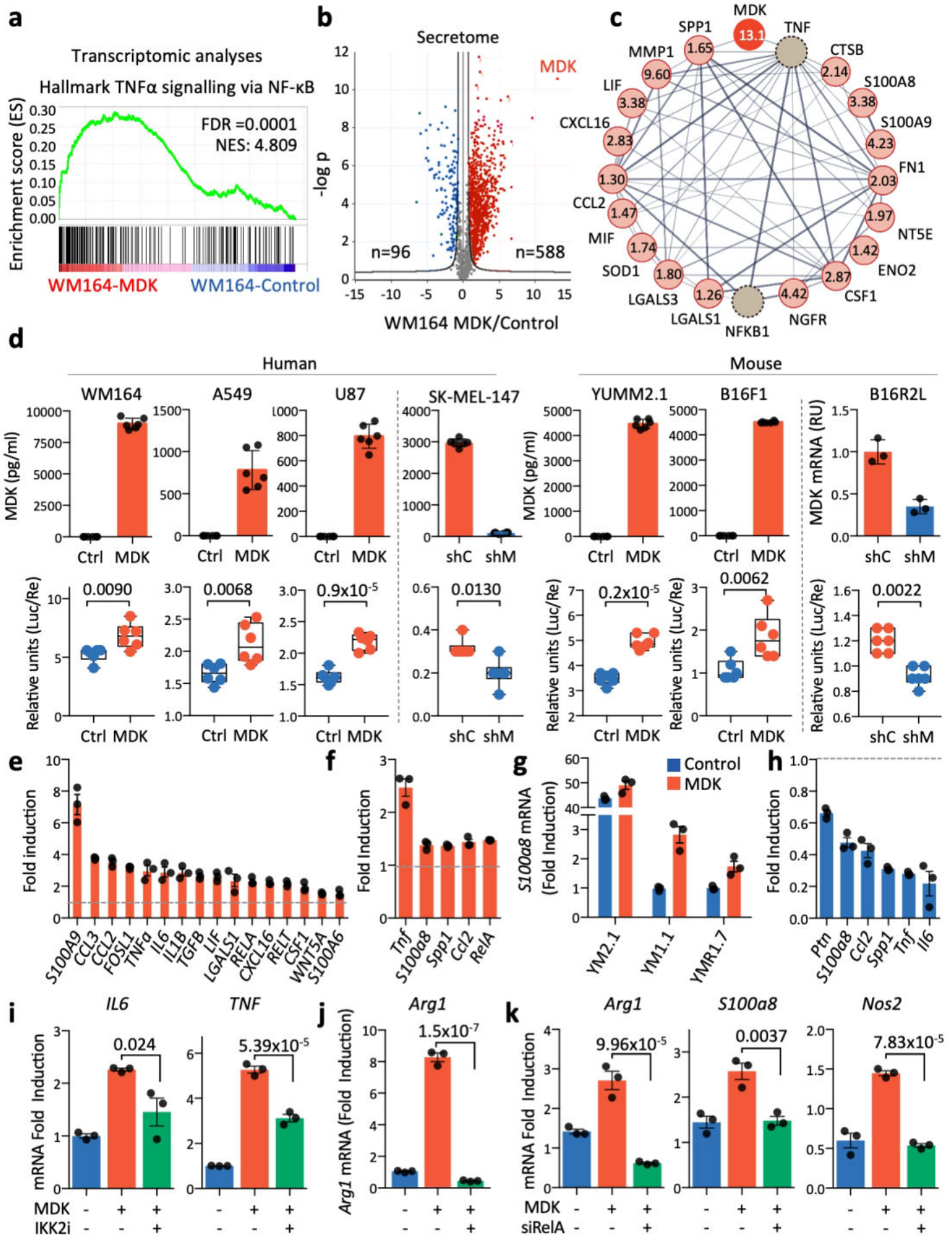

Cerezo-Wallis et al. Figure 4

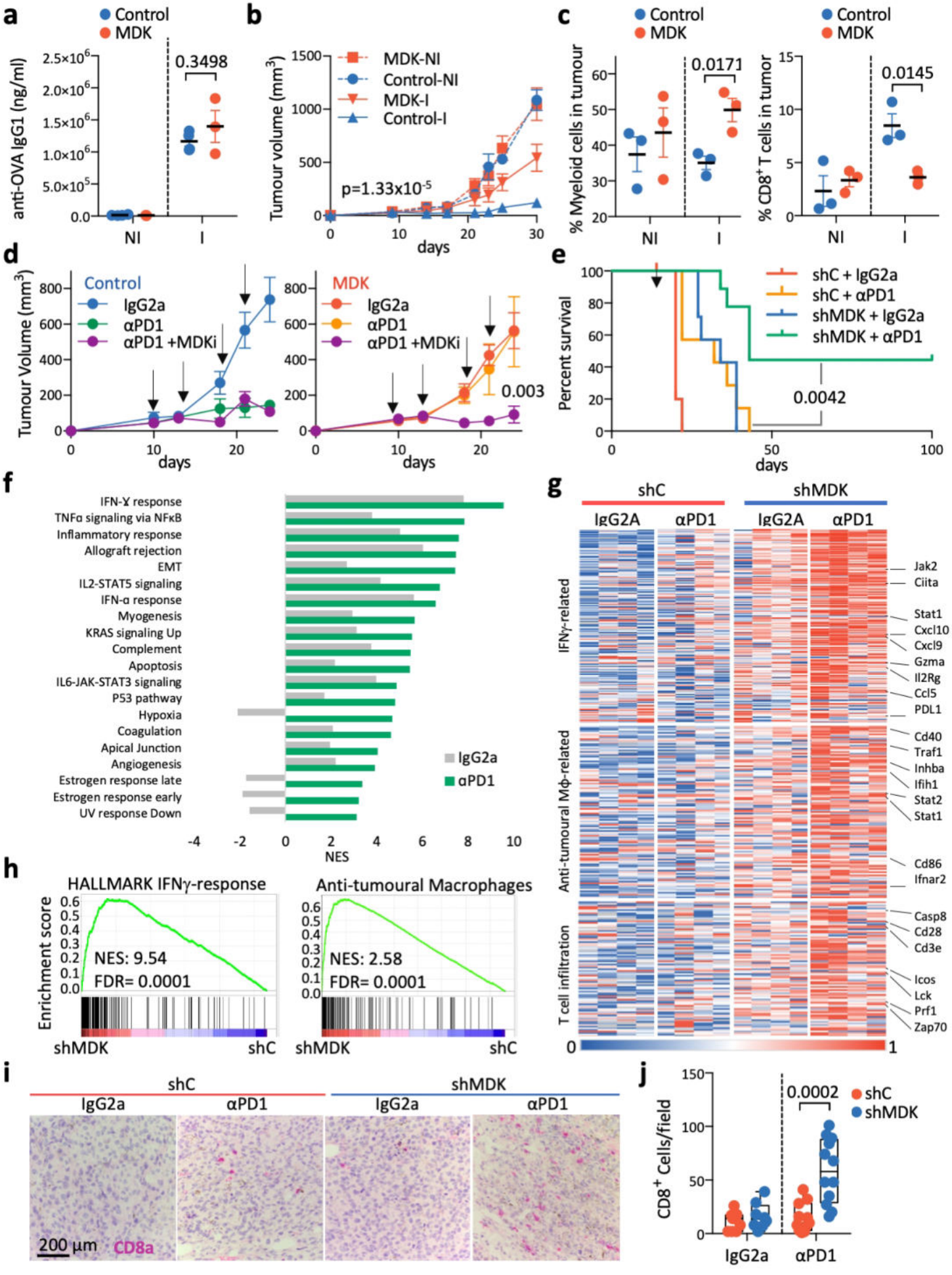

Cerezo-Wallis et al. Figure 5

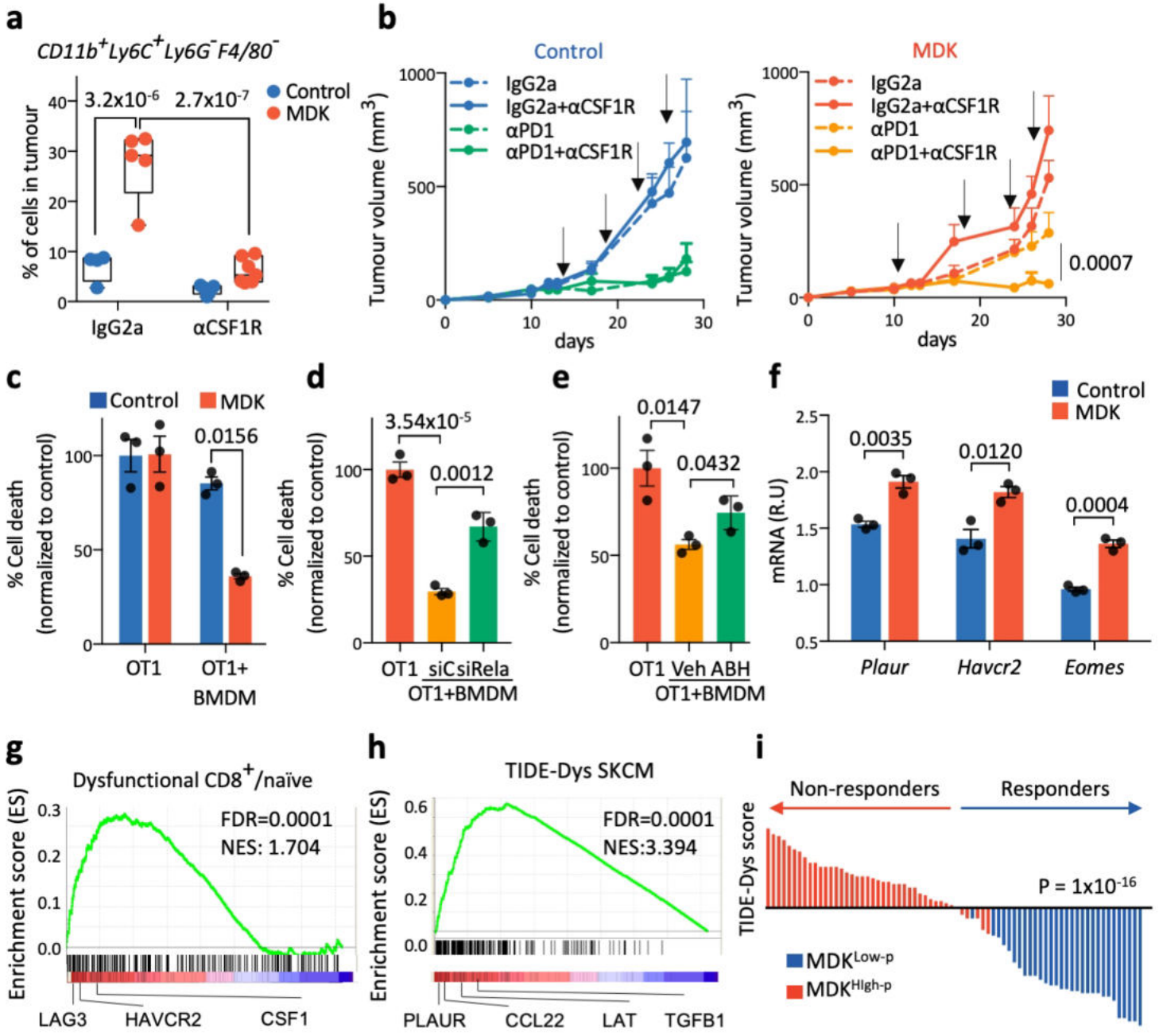

Cerezo-Wallis et al. Figure 6

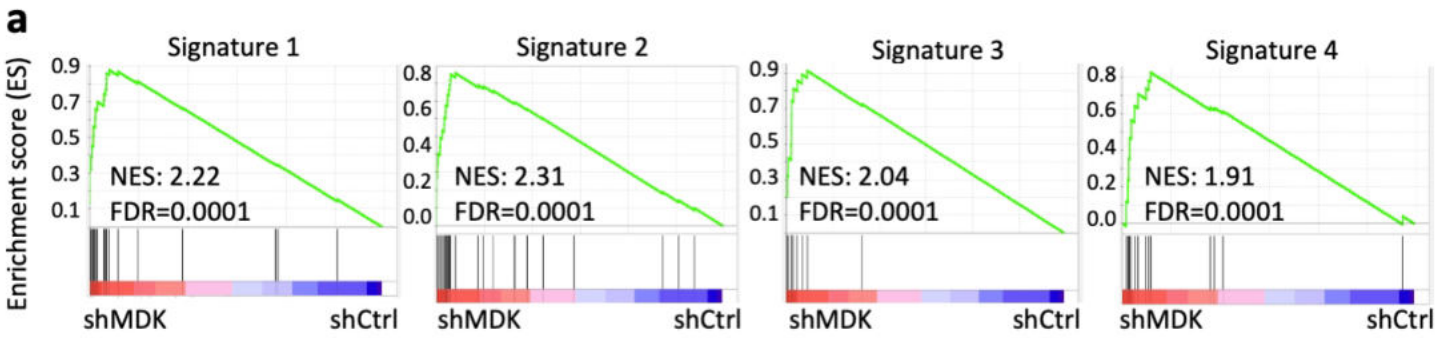

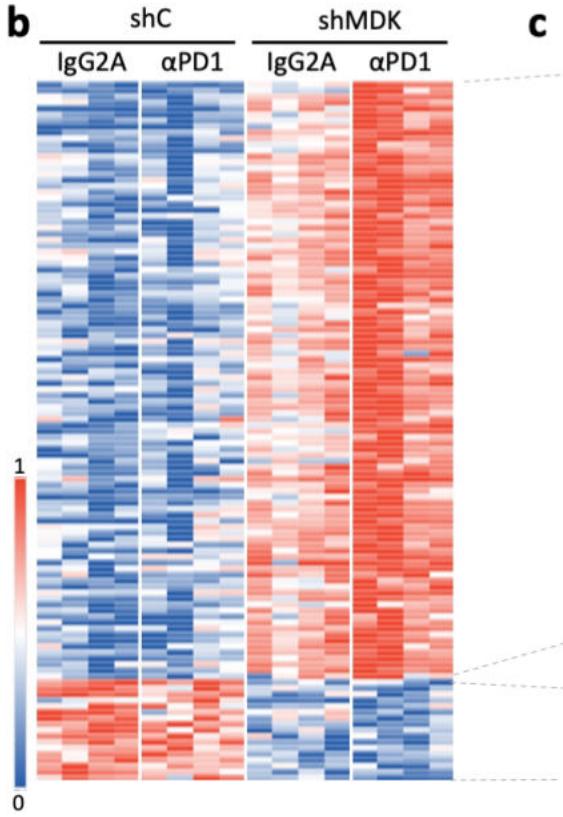

c

Shared	This study	
RASSF5	PLEK	DSP
UBD (2)	CD300LF	CD300LB
GZMA (1, 2, 6, 8)	TGFBI	SLFN5
IRF5 (6)	MARCHF1	RUNX3
SERPING1 (6)	MAFB	MYO1F
IL2RB (6, 8)	C4B	CTSH
SLC15A3 (7)	PTAFR	RGS2
CSF2RB (6)	SERPINB9	CCL15
CD3D (1, 3, 8)	VSIR	IER5
ITGB7 (6)	PTPRCAP	MCUB
TRAFD1 (6)	AHNAK	DOK2
IRF7 (6, 8)	ENTPD1	IFI27L2
TNFRSF1B (7)	LST1	HK3
FGR (5)	MS4A4E	PLBD1
SYK (7)	CYP4F3	MNDA
AIM2 (2)	TREM2	SMIM3
RGS1 (8)	SLFN12	NCF1
SP110 (6)	SPI1	CD83
TRBC2 (5)	LILRA4	TMEM106A
EBI3 (7)	SDC3	RNF19B
	CCR2	CLEC6A

Shared	This study		
	MDK	SNRPF	SOX5
	DHRS2	ABCA12	NCAM1
	IPPK	FBLN5	SPRY2

e

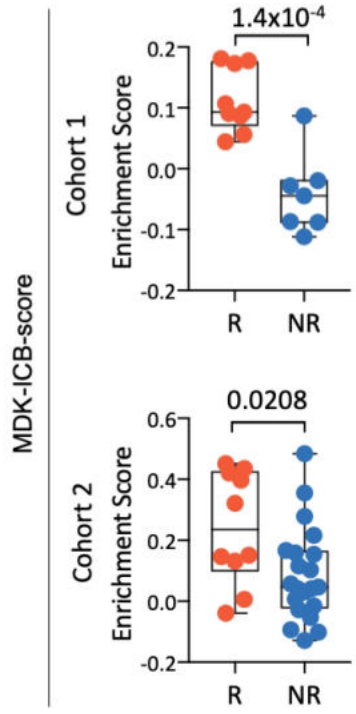

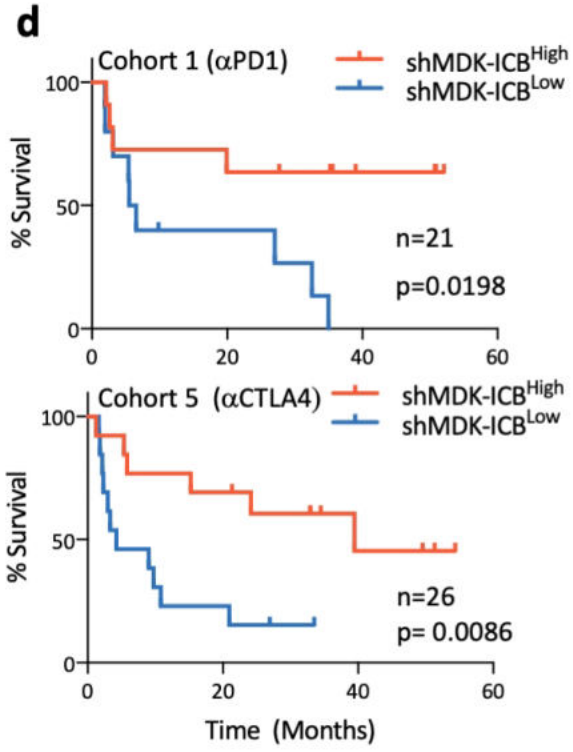

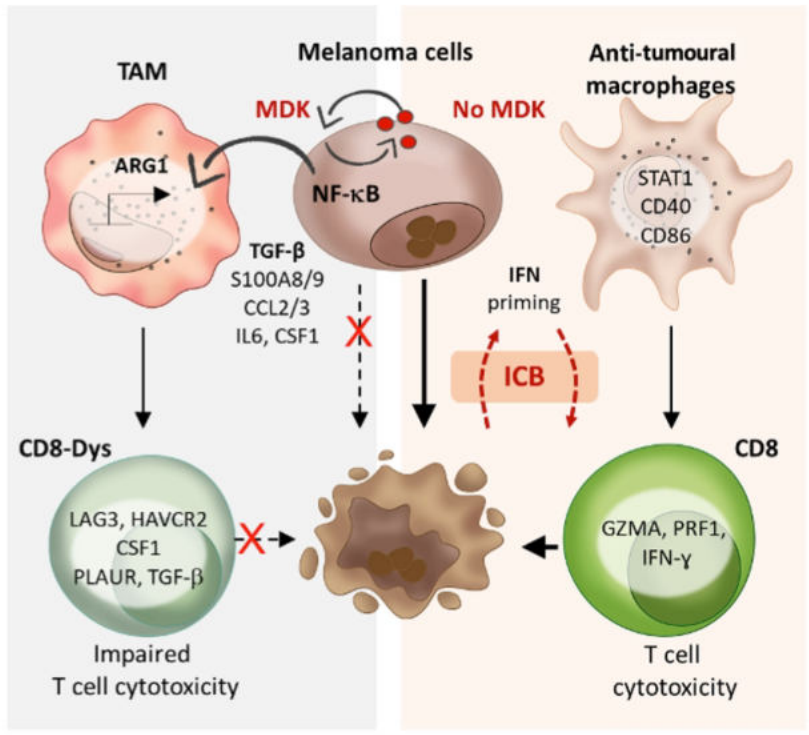

Cerezo-Wallis et al. Supplementary Figure 1

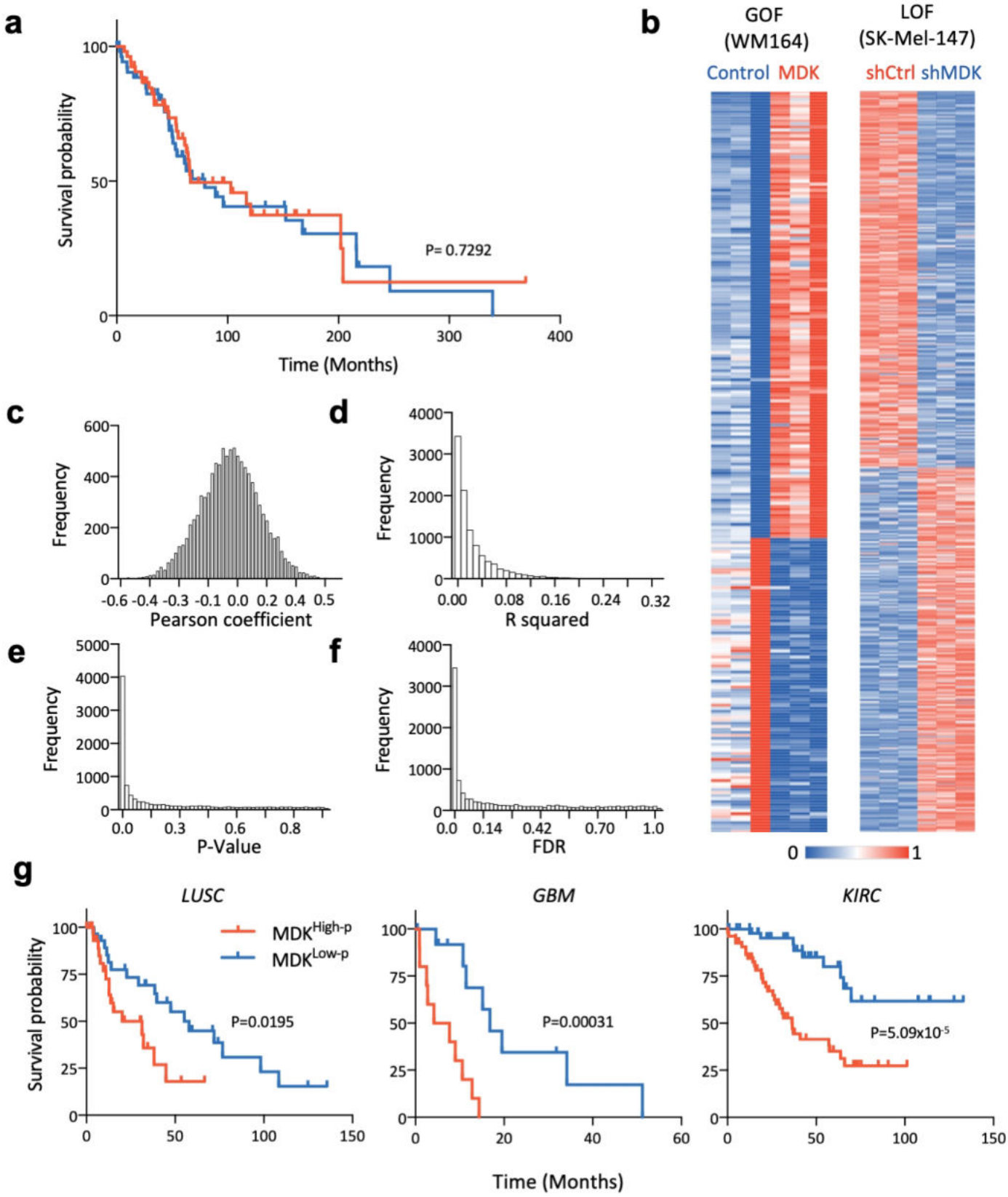

Cerezo-Wallis et al. Extended Fig 2

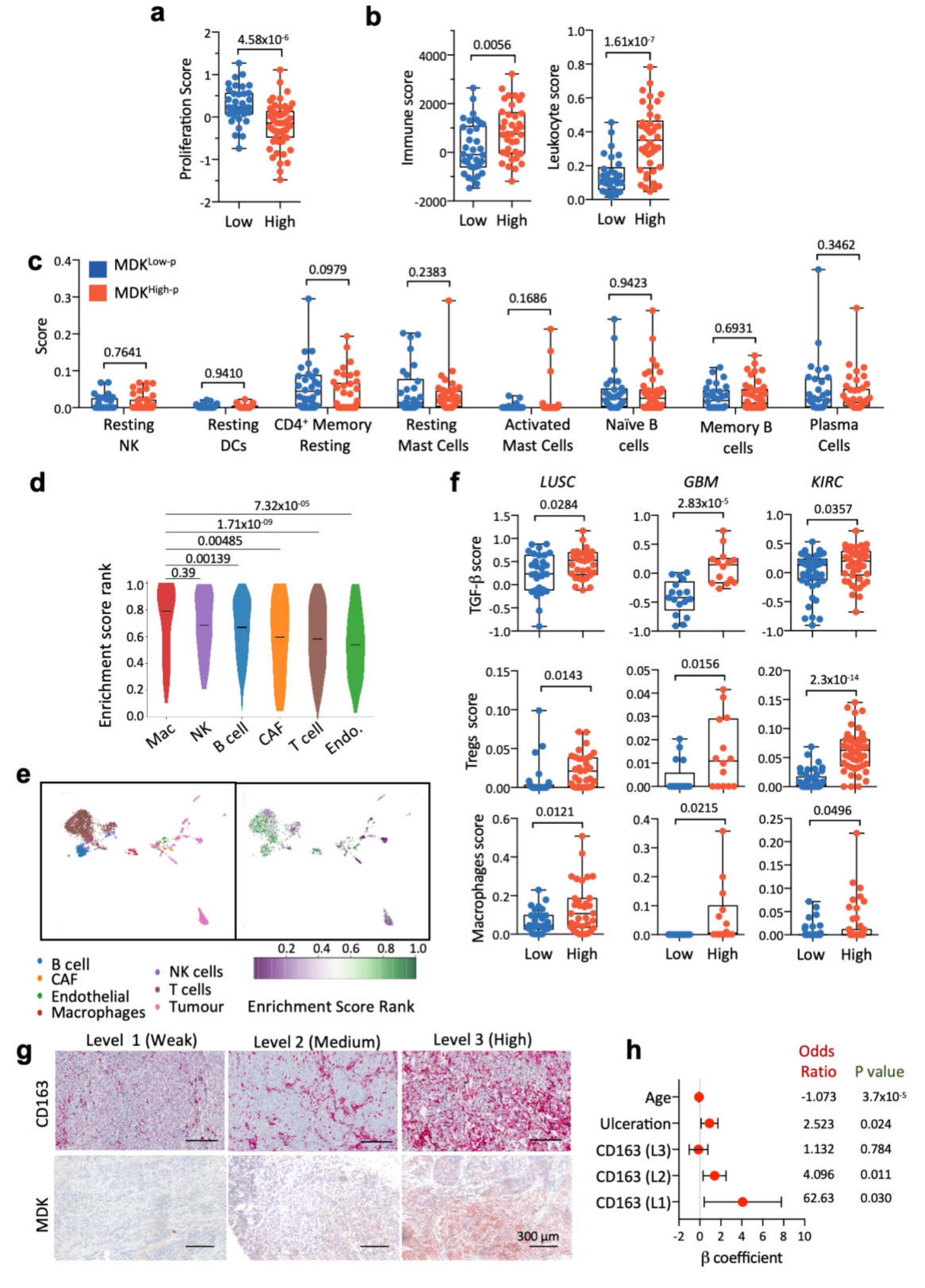

Cerezo-Wallis et al. Extended Figure 3

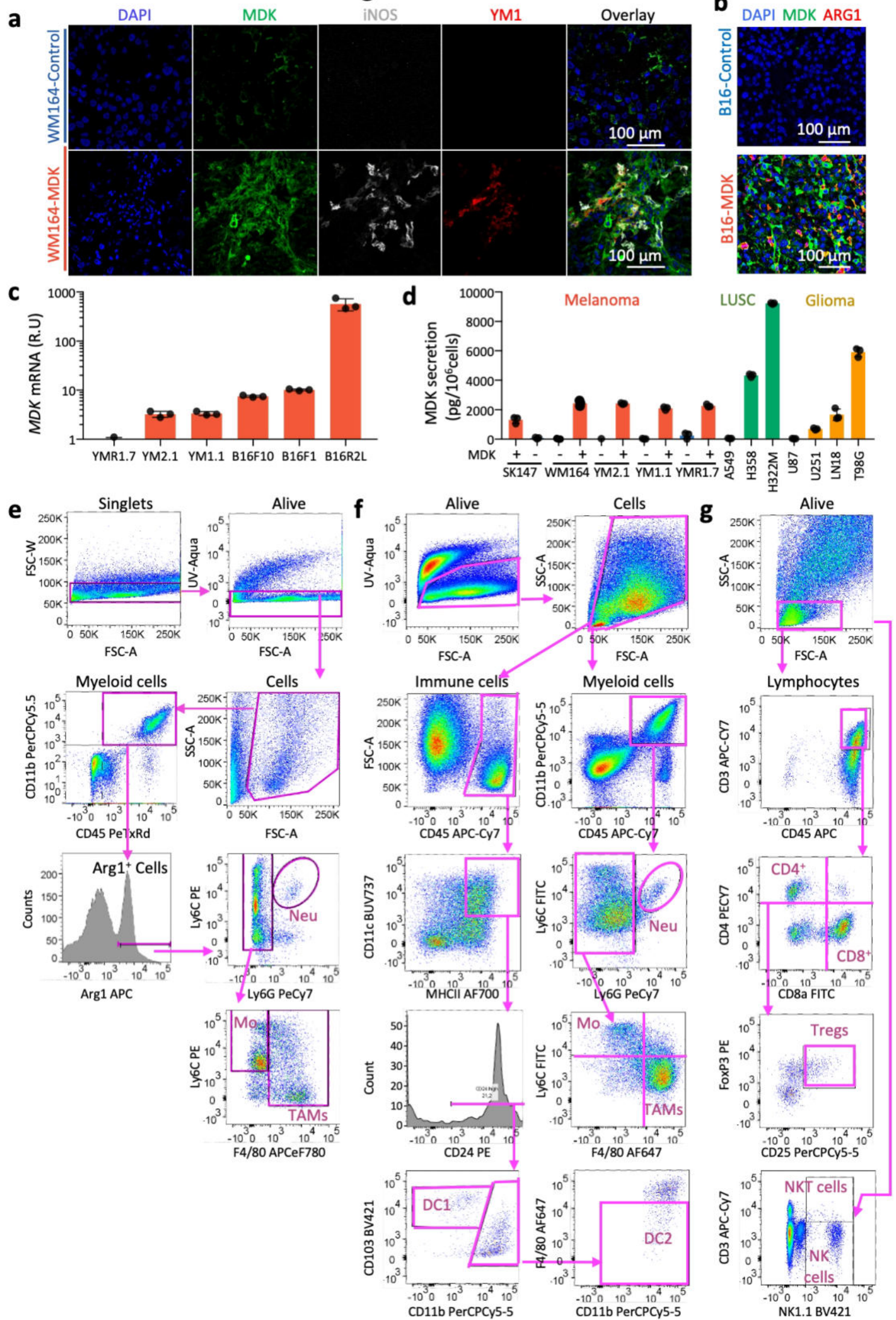

Cerezo-Wallis et al. Extended Figure 4

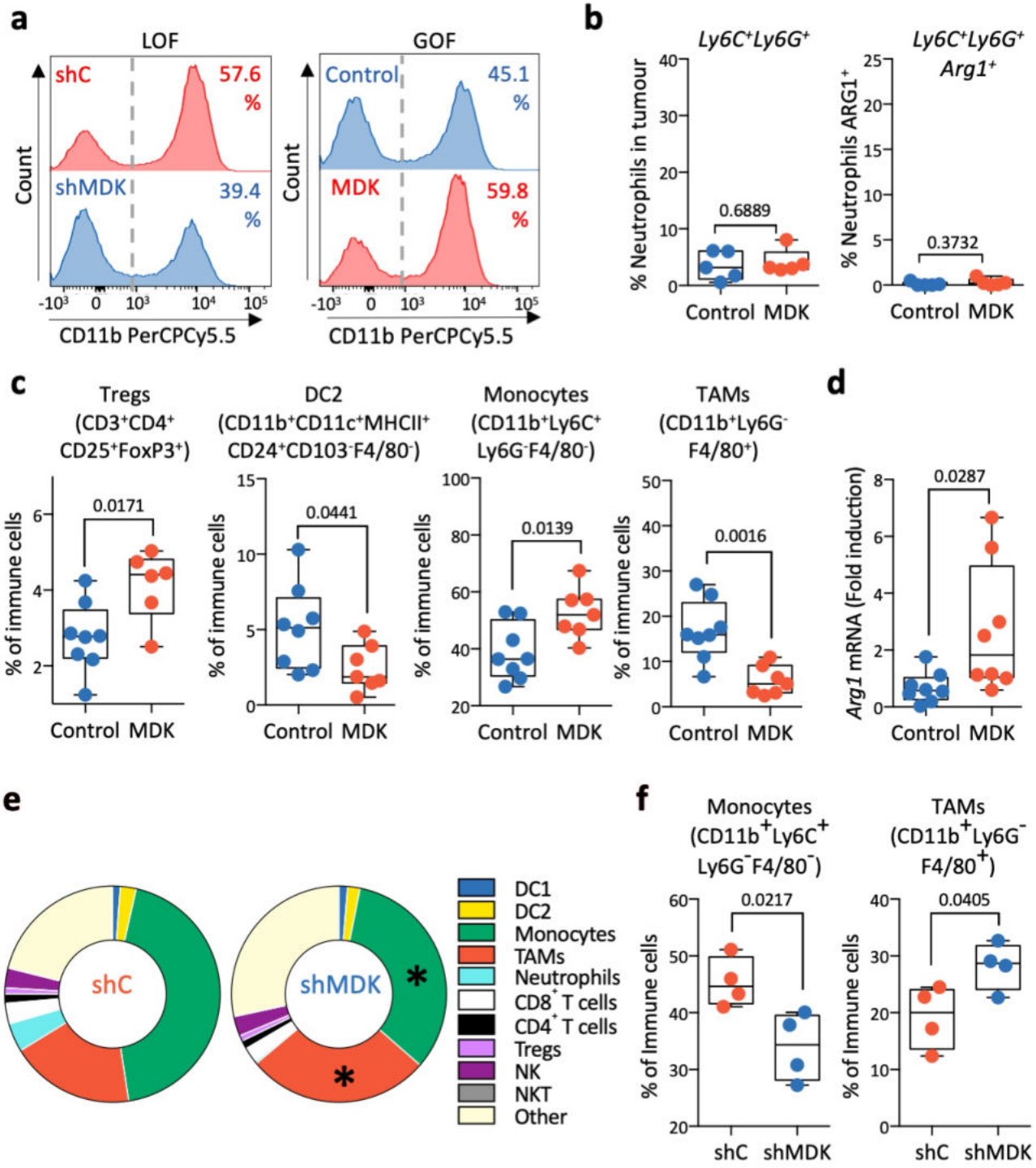

Cerezo-Wallis et al. Extended Figure 5

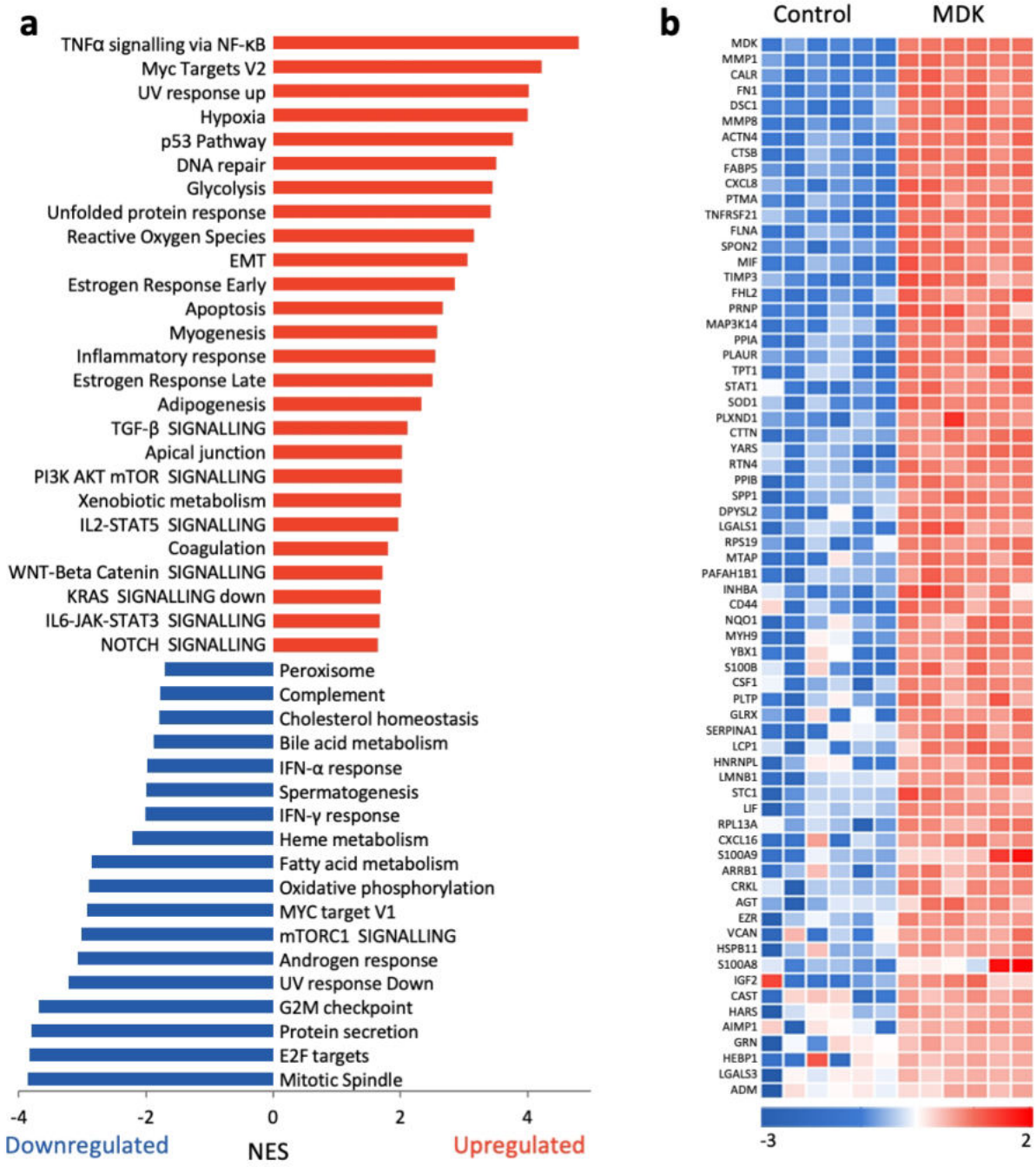

Cerezo-Wallis et al. Extended Figure 6

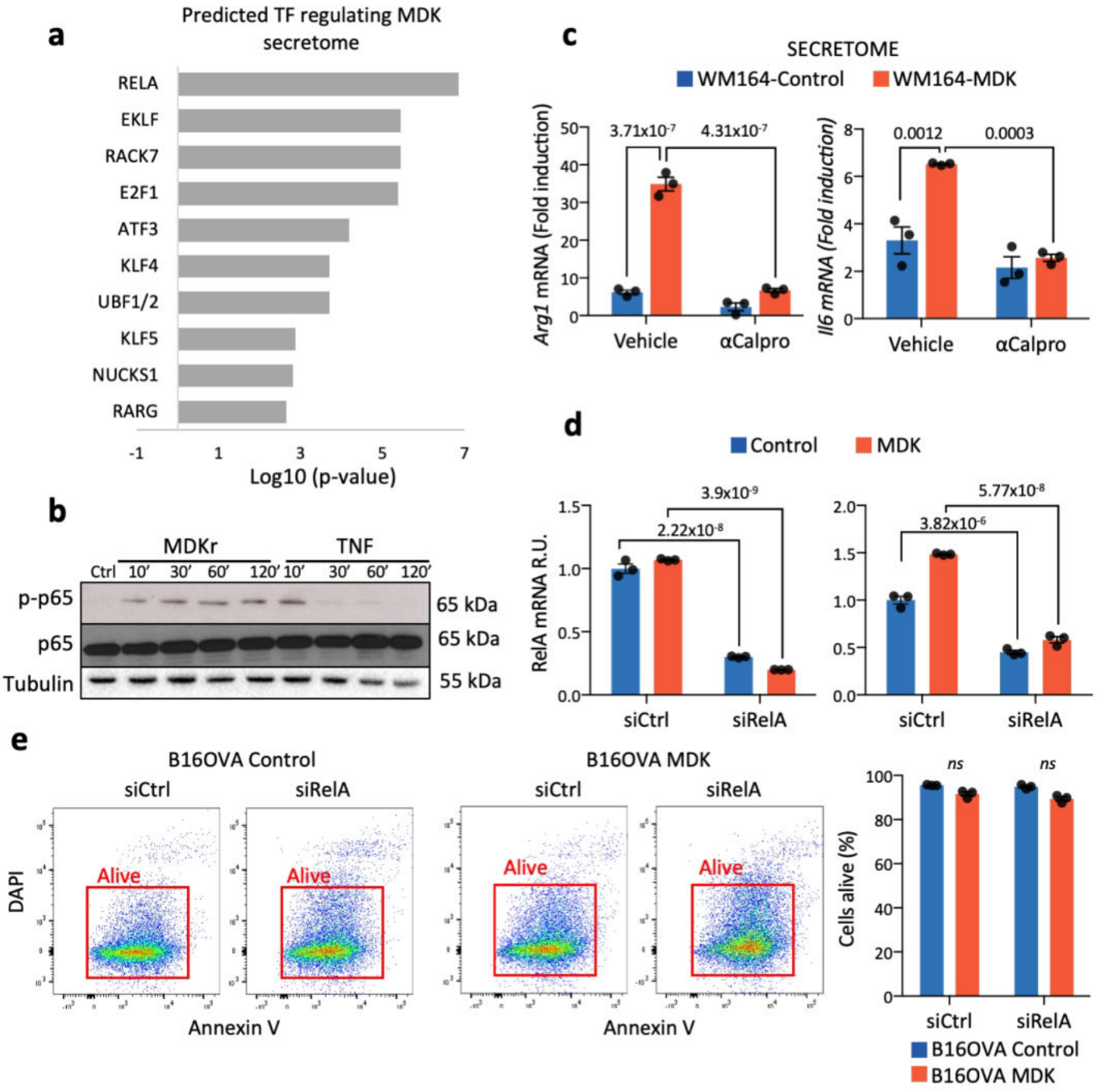

Cerezo-Wallis et al. Extended Figure 7

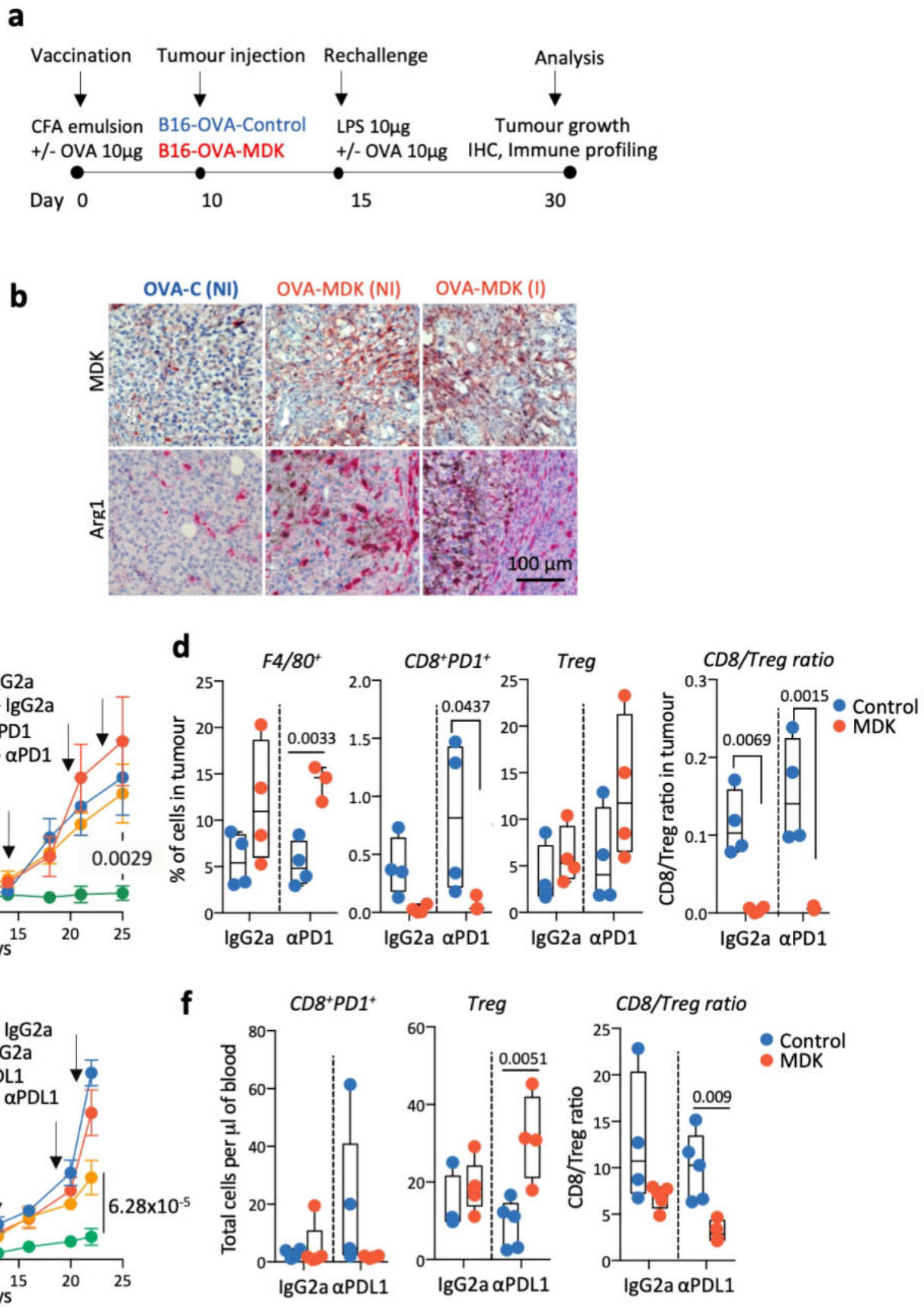

Cerezo-Wallis et al. Extended Figure 8

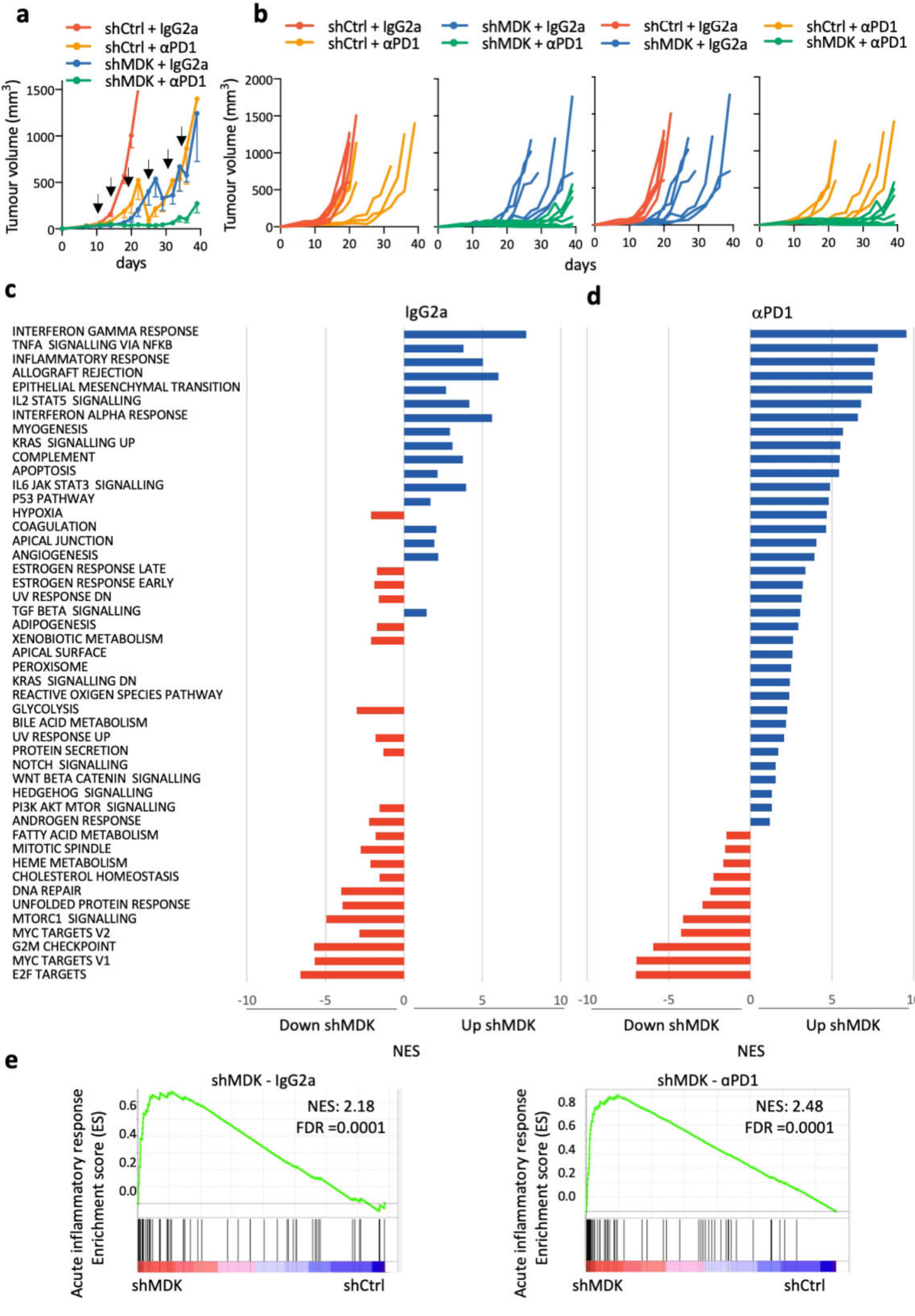

Cerezo-Wallis et al. Extended Figure 9

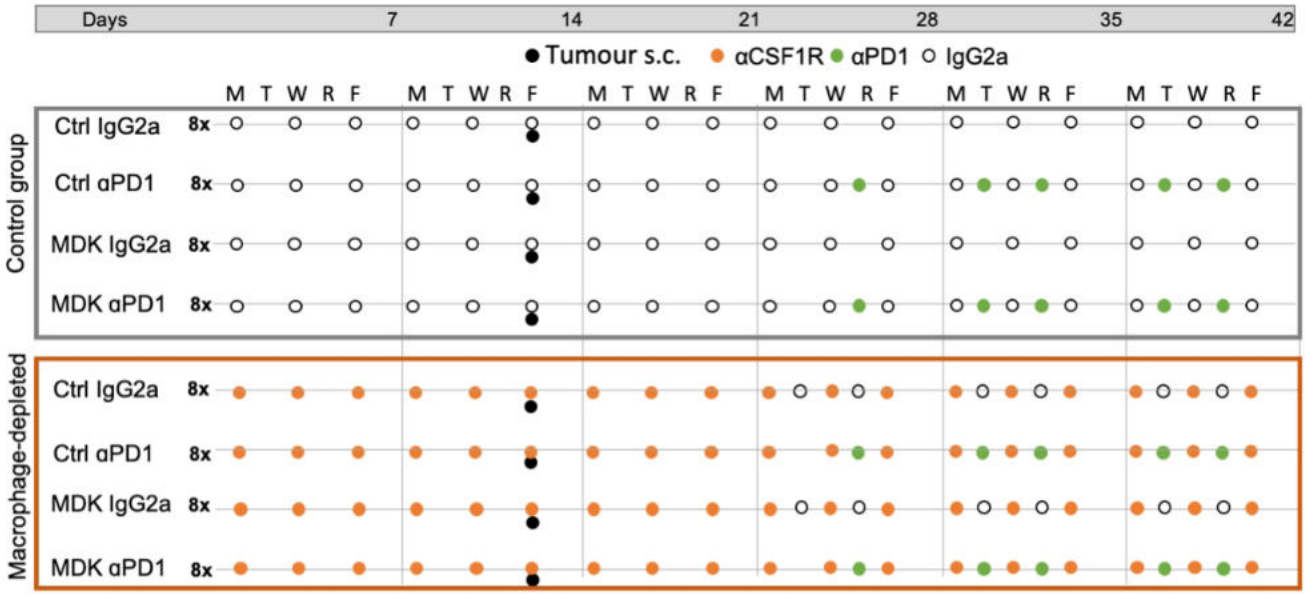

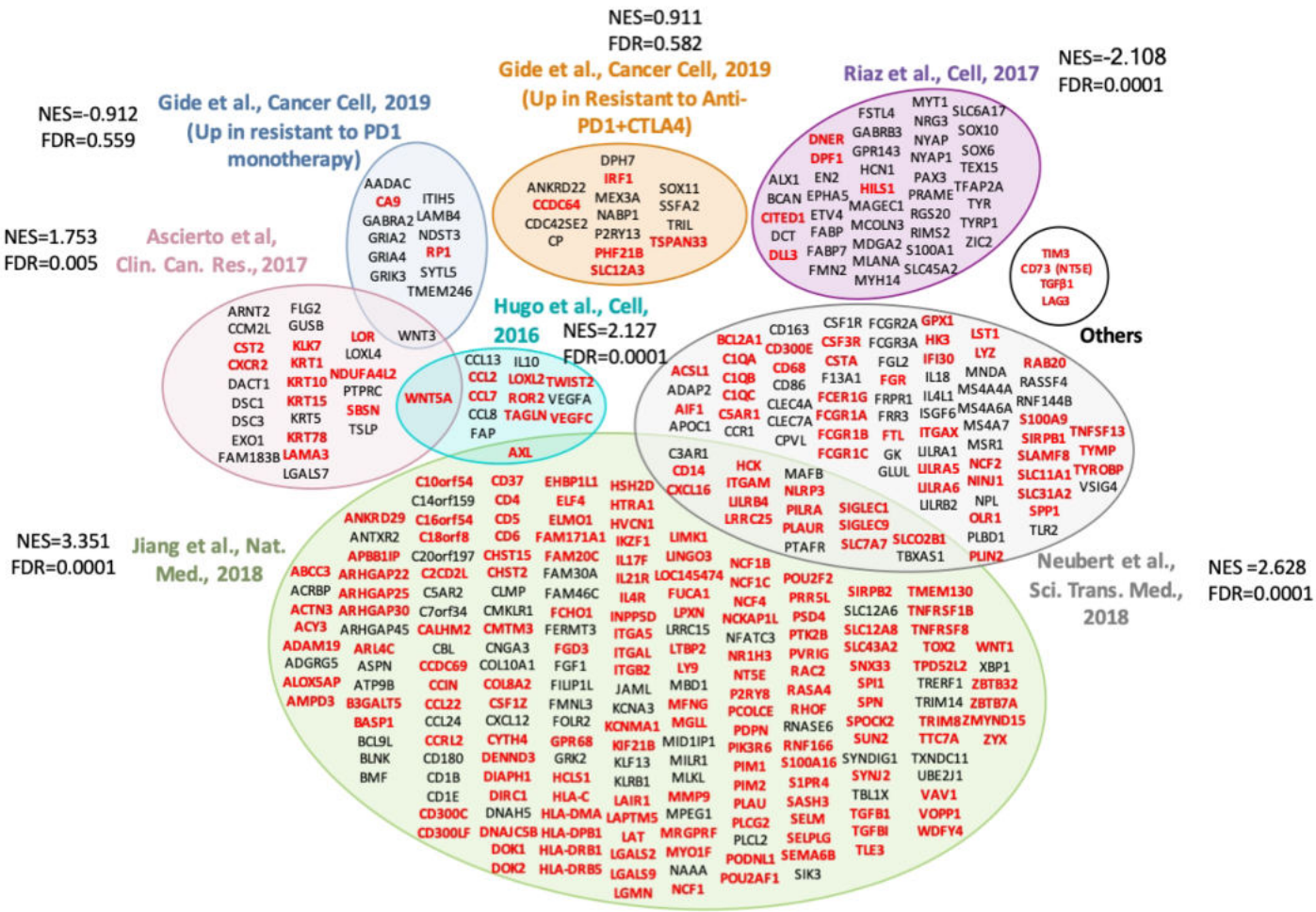

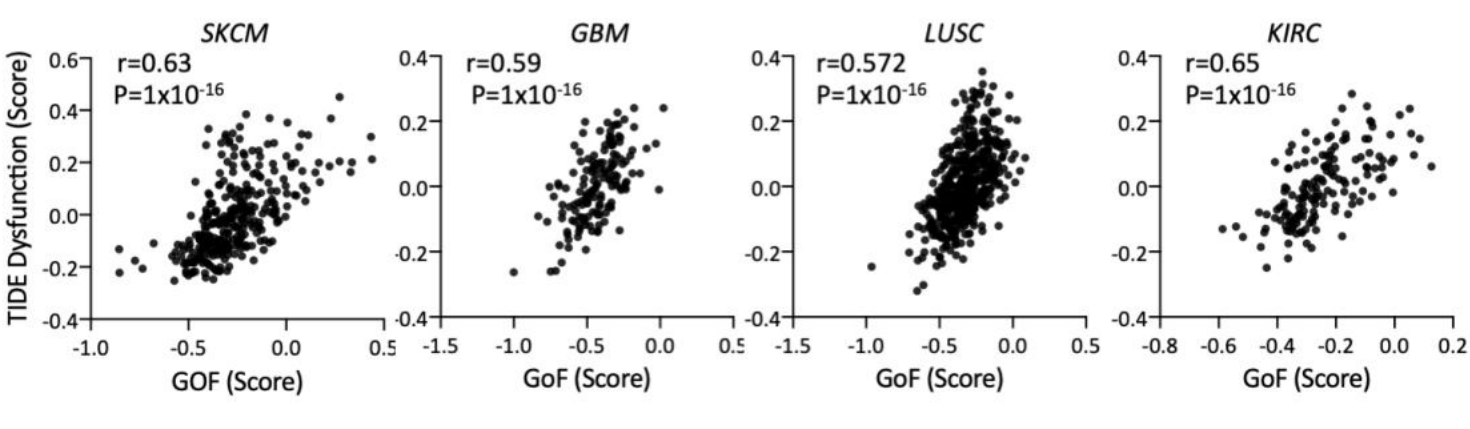

Cerezo-Wallis et al. Extended Figure 10